

Ab initio screening of quantum frustrated materials with kagome and triangular geometries

Byeong-Hyeon Jeong, Hee Seung Kim, SungBin Lee,* and Myung Joon Han†

Department of Physics, Korea Advanced Institute of Science and Technology (KAIST), Daejeon, South Korea

(Dated: March 16, 2026)

Geometrical frustration is a powerful route to realize exotic phases such as quantum spin liquids. Despite extensive efforts, systematic searches targeting specific frustration motifs and their potential to host unconventional magnetic ground states remain rare, thus highlighting the need for a more focused and predictive materials discovery approach. Here we present a new strategy combining high-throughput first-principles calculations, magnetic force theory, and spin Hamiltonian analysis. Starting from the $\sim 150,000$ material database, we catalogue candidate materials that may host competing exchange interactions and new types of magnetic states with the focus on kagome or triangular lattices. Our workflow not only reproduces the majority of known frustrated magnetic materials, validating our approach, but also predicts novel candidate compounds with targeted frustration profiles that have not yet been experimentally synthesized. Among these, we identify six promising new materials: one triangular lattice compound, KMgNiO_6 , and five kagome lattice compounds— $\text{Li}_4\text{Fe}_3\text{WO}_8$, $\text{Li}_2\text{V}_3\text{F}_8$, $\text{Li}_5\text{VP}_2(\text{O}_4\text{F})_2$, and $\text{Li}_2\text{MgCo}_3\text{O}_8$ ($P2/m$ and $C2/m$). For each candidate, we identify detailed magnetic properties and further propose their potential magnetic ground states, revealing that some of them may host entirely new magnetic phases driven by their distinct frustration characteristics.

I. INTRODUCTION

Geometrical frustration arises when spins fail to simultaneously minimize their exchange energy owing to competing interactions. This phenomenon has attracted considerable interest due to its potential to host unconventional magnetic orders or quantum spin liquids (QSLs), characterized by long-range quantum entanglement and fractionalized excitations [1–5]. Consequently, the search for frustrated magnetic materials capable of realizing such exotic ground states has remained a central focus of condensed matter physics. Over the past few decades, sustained efforts have been directed toward both the experimental discovery and the theoretical investigation. Despite these efforts, the identification of genuine frustrated magnetic systems remains a topic of active debate [1–6]. It highlights the longstanding need for systematic approaches to identify frustrated magnets in a controlled and predictive manner.

To date, most theoretical and computational efforts have focused on understanding the magnetic properties of already synthesized materials. A wide range of tools have been successfully employed to characterize known systems and uncover their natures. While these approaches have provided valuable insights, they offer limited guidance for the new materials discovery. A systematic framework and a corresponding workflow have yet to be established. Although high-throughput screenings based on the extensive material database and density functional theory (DFT) calculations have been successful for various cases [7–18], it has been severely limited for this case of strongly correlated electron phenomena [19, 20]. The targeted search for

specific forms of frustration remains largely unexplored.

In this study, we establish a systematic, multi-step workflow for the discovery of novel frustrated magnetic materials, combining high-throughput screening with first-principles calculations, magnetic force theory, and spin Hamiltonian analysis. This approach enables the targeted identification of specific magnetic frustration emerging from lattice geometry and competing exchange interactions. We focus on triangular and kagome lattice compounds with partially filled $3d$ transition metal (TM) ions. Notably, our framework successfully rediscovers many well-established QSL candidates, including such kagome systems as herbertsmithite, kapellasite, Vesignieite, and Volborthite. Also identified are triangular lattice compounds, including NiGa_2S_4 , $\text{Ba}_3\text{NiSb}_2\text{O}_9$ (6H-B phase), and delafossite-like AgCrSe_2 . The successful identification of these benchmark materials validates the robustness and reliability of our approach.

Further, our workflow uncovers previously unexplored compounds predicted to exhibit strong frustration. These include a triangular lattice compound, KMgNiO_6 , and five kagome lattice candidates: $\text{Li}_4\text{Fe}_3\text{WO}_8$, $\text{Li}_2\text{V}_3\text{F}_8$, $\text{Li}_5\text{VP}_2(\text{O}_4\text{F})_2$, and two symmetry-inequivalent forms of $\text{Li}_2\text{MgCo}_3\text{O}_8$ with $P2/m$ and $C2/m$ space groups. These results demonstrate the power of systematic, data-driven search in guiding the discovery of new frustrated magnets and spin liquid candidates. For each candidate, we assign the most probable ordered manifold. The newly predicted materials are strong candidates to host not only conventional coplanar orders ($q = 0$) but also noncoplanar cuboc states, including the newly identified ‘cuboc-3’ region. Our workflow provides (i) a validated, data-driven searching strategy, (ii) an experimentally actionable shortlist of frustrated magnets with quantified exchange hierarchies, and (iii) clear model-level diagnoses to guide synthesis and characterization.

* sungbin@kaist.ac.kr

† mj.han@kaist.ac.kr

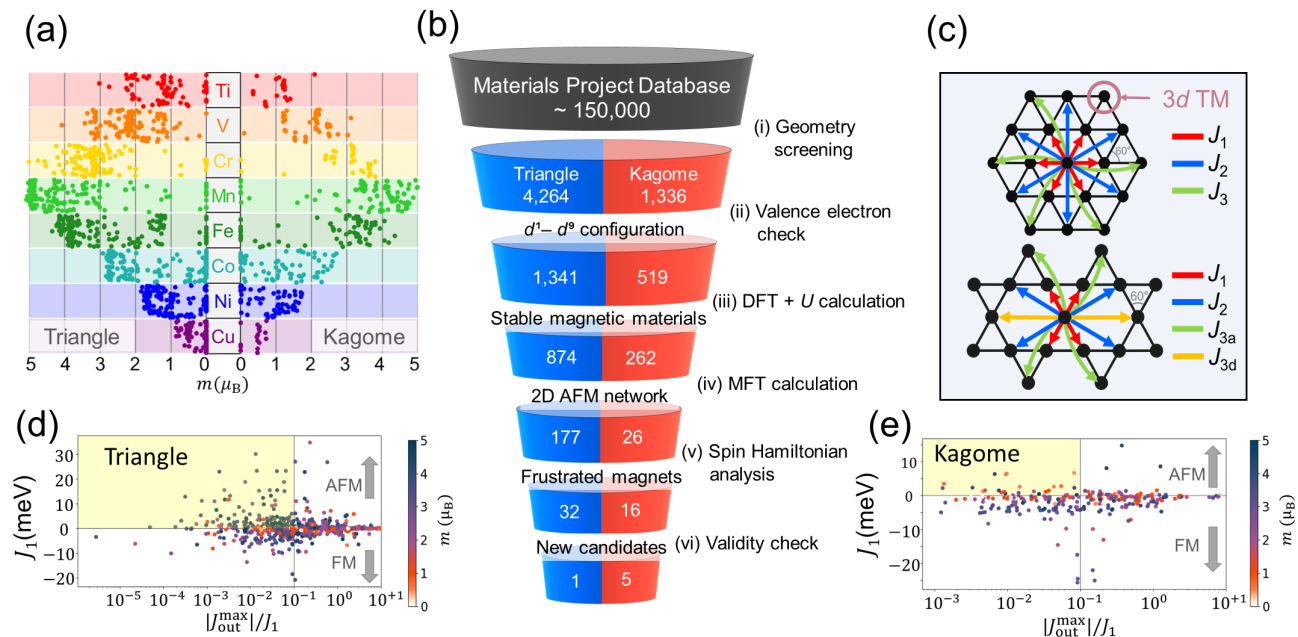


FIG. 1. (a) Calculated magnetic moments at TM sites for 1,653 materials yielding stable magnetic solutions. (b) Schematic overview of the multi-step high-throughput screening workflow and the corresponding results. Starting from a database of 154,713 materials, the procedure ultimately provides the catalog of frustrated magnetic materials and identifies the six strongest candidates which have not yet been synthesized. (c) Crystal structures and associated intra-layer exchange interactions for triangular and kagome lattices. (d, e) Calculated J_1 values and their ratios with respect to the largest inter-layer coupling ($J_{\text{out}}^{\text{max}}$). The yellow-shaded region indicates the screening threshold $|J_{\text{out}}^{\text{max}}| \leq 0.1J_1$ (with AFM J_1). Panels (d) and (e) present results for triangular and kagome systems, respectively. By convention, positive (negative) J corresponds to antiferromagnetic (ferromagnetic) interactions.

II. THE HIGH-THROUGHPUT SCREENING WORKFLOW

Our material-search workflow consists of six steps, as shown in Fig. 1(b). Here we outline the main idea and the computational details are provided in Computation Details section.

A. Database search and the screening for geometrical property

We first search a well-established material database for candidate materials. In the current work, we focus on two lattice systems, namely kagome and triangular lattices, and use the Materials Project database [21], which contains 154,713 materials. Importantly, it includes both experimentally synthesized and unsynthesized materials. For kagome lattice systems as an example, our screening criteria include (see Fig. 1(c)): (a) Each kagome site should have four nearest neighbors (NNs). (b) Bond angles between two NN sites should be given by either 60° , 120° , or 180° . Similarly, for the triangular system, each site has six NNs, and the bond angles are six of 60° , six of 120° , and three of 180° . Since some obviously irrelevant materials can also satisfy these conditions, we perform an additional ‘planarity check’ to ensure that all these atoms

lie within a single plane. To account for unavoidable uncertainties and possible database errors, we introduce tolerances of up to 4° in bond angles and up to 6% in bond lengths [22].

B. Screening based on the valence configuration

From the initial screening step, we obtained 4,264 triangular and 1,336 kagome materials with $3d$ TMs occupying the primary sites. By considering the oxidation states of the TM ions, we further excluded compounds with $3d^0$ or $3d^{10}$ electronic configurations. The valence states were determined using the tool described in Ref. [23]. In addition, we removed materials in which multiple atomic species simultaneously possess partially filled d -orbitals; such systems merit further investigation in future studies. After these refinements, our screening yielded 1,341 triangular lattice and 519 kagome lattice candidate materials.

C. DFT+ U calculation

The third step involves DFT+ U calculations for 1,860 ($= 1,341 + 519$) candidates since the materials of interest lie well within the strongly correlated regime. The primary goal of this DFT+ U step is to obtain the full-band

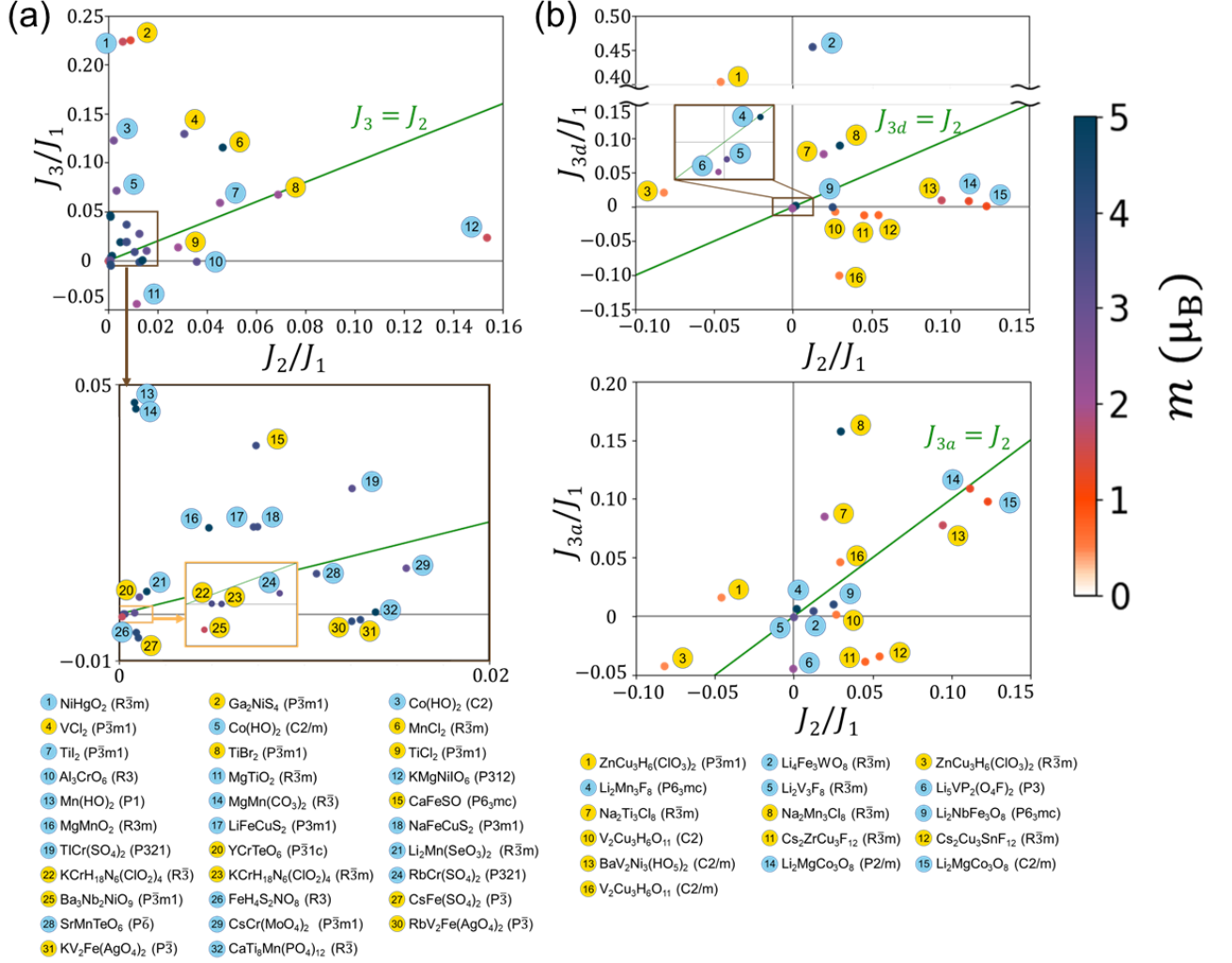


FIG. 2. Catalog of (a) triangular and (b) kagome lattice compounds situated in the magnetically frustrated regime, plotted in the J_2/J_1 – J_3/J_1 parameter space. Each numbered marker corresponds to a specific material, with yellow circles indicating compounds that have been experimentally synthesized and blue circles representing unsynthesized candidates. The color scale denotes the calculated ordered magnetic moment m (in μ_B). Green lines mark the condition $J_{3(a/d)} = J_2$, and magnified insets highlight regions with dense data distributions.

Hamiltonian and spin-dependent charge density. However, it also serves as a further screening stage: materials whose self-consistent solutions converge to a nonmagnetic state or to a configuration with nonuniform magnetic moments were excluded. We retained only those systems that converged reliably to symmetry-preserving solutions with nonzero magnetic moments. As a result, 874 triangular and 262 kagome lattice materials were selected. The calculated magnetic moments of these compounds are presented in Fig. 1(a).

D. MFT calculation

We extract the magnetic coupling constants by applying the magnetic force theorem (MFT) within linear response theory [24–27]. For conventional Heisenberg spin

Hamiltonian, $H = -J_{ij}\mathbf{S}_i \cdot \mathbf{S}_j$, MFT estimates

$$J_{ij}(\mathbf{q}) = \frac{1}{\pi} \text{Im} \int^{\epsilon_F} d\epsilon \int_{\text{B.Z.}} d\mathbf{k} \text{Tr}[\mathbf{V}_{\mathbf{k},i} \mathbf{G}_{\mathbf{k},ij} \mathbf{V}_{\mathbf{k}+\mathbf{q},j} \mathbf{G}_{\mathbf{k}+\mathbf{q},ji}], \quad (1)$$

and its Fourier transform gives rise to J_i . $\mathbf{G}_{\mathbf{k},ij}$ is Green's function propagator, and $\mathbf{V}_{\mathbf{k},i}$ represents spin perturbation. MFT enables us to avoid the multiple total-energy calculations of enlarged supercells which are not well compatible with high-throughput screening workflow.

The calculation results are presented in Fig. 1(d) and (e) in terms of the averaged NN exchanges, J_1 , and the maximum out-of-plane value ($J_{\text{out}}^{\text{max}}$). Before conducting further analyses in the following step, we discard the materials unless they have major AFM couplings and the well-defined 2D triangular/kagome plane: namely, (i) $J_1 > 0$ and (ii) $|J_{\text{out}}^{\text{max}}/J_1| < 0.1$. The selected materials

are the ones that fall into the yellow-colored regions in Fig. 1(d) and (e); 177 triangular and 26 kagome materials.

E. Spin Hamiltonian analysis – Screening of exchange interactions

We next identify compounds with strongly competing exchange interactions. This step is critical: although triangular or kagome connectivity provides the geometric precondition for frustration, further-neighbor competition can substantially enhance it. Because such competition cannot be captured by a single parameter, our fifth screening stage adopts a broader, multi-metric evaluation.

For triangular lattices, previous studies have explored the enhanced frustration conditions in terms of J_1 and J_2 [28–36]. For instance, in the simple spin-1/2 J_1 Heisenberg model, the ground state is characterized by 120° magnetic order. However, the introduction of a small but positive J_2 ($0.08 \lesssim J_2 \lesssim 0.16$) stabilizes a QSL phase. Motivated by this, we apply screening criteria requiring $J_2 > 0$ and $|J_1^{\text{avg}}| > |J_{2,3}^{\text{avg}}|$. To account for inevitable numerical deviations and potential database inaccuracies, we allow the standard deviation of J_1 values to be as large as 25% of J_1^{avg} —a tolerance required to maintain the stability of well-established compounds. Furthermore, we verify at this stage that the converged solutions are insulating and that the total energy calculations favor antiferromagnetic states. Applying this sequence of screening conditions reduces the pool of candidate triangular materials from 177 to 32, as summarized in Fig. 2(a).

For kagome lattices, the J_1 Heisenberg model is widely believed to host a spin-liquid ground state. When further-neighbor interactions are introduced, previous studies have shown that the system remains highly frustrated and does not develop long-range magnetic order, irrespective of the sign of J_2 , provided its magnitude is small [37–42]. Accordingly, we do not impose any restriction on the sign of J_2 in our screening procedure. For total energy comparisons, we adopt the two-up-one-down spin configuration. With these criteria, we identify 16 kagome candidates, listed in Fig. 2(b), which will be subjected to further analysis in the next step.

F. The final selection and the validity check

Among the 32 triangular systems, 13 have already been synthesized experimentally, including well-established compounds that reinforce the validity of our screening workflow. For the 19 unsynthesized candidates, we analyze their magnetic coupling profiles in detail, guided by previous model studies [28–36]. In particular, we focus on the criterion $J_2 \gtrsim 0.08$, where the conventional 120° magnetic order is expected to be destabilized. Among the unsynthesized, KMgNiO_6 ($R\bar{3}m$, #9) emerges as the only promising candidate for which we perform a series of additional check calculations considering the known

limitations of conventional DFT+ U methodology (see Computation Details section and Appendix). This material is finally selected.

As for kagome systems, 9 out of the 16 candidates have already been synthesized experimentally. This list again includes well-known QSL candidates such as Herbertsmithite and Volborthite, further supporting the robustness of our approach. For the 7 unsynthesized kagome materials, we carry out detailed investigations. The same validation check procedure with different DFT functional choices and interaction parameters excludes two: $\text{Li}_2\text{Mn}_3\text{F}_8$ ($P6_3mc$, #4) and $\text{Li}_2\text{Nb}_3\text{Fe}_3\text{O}_8$ ($P6_3mc$, #9).

For the final list of six new materials (1 triangular + 5 kagome; see Table I), further discussion will be discussed in the following section.

III. RESULTS

A. Catalog of triangular materials

Following the workflow described above, the selected 32 triangular materials are expected to host well-defined triangular spin lattices localized on the transition-metal ions, exhibit insulating gaps, and feature two dominant competing antiferromagnetic interactions ($J_{1,2} > 0$).

Among the 13 synthesized compounds highlighted in Fig. 2(a) by yellow labels, 120° AFM order has been reported for VCl_2 ($P\bar{3}m1$, #4), TiCl_2 ($R\bar{3}m$, #9), CaFeSO ($P\bar{3}$, #15), $\text{Ba}_3\text{Nb}_2\text{NiO}_9$ ($P\bar{3}m1$, #25), $\text{CsFe}(\text{SO}_4)_2$ ($P\bar{3}$, #27), $\text{RbV}_2\text{Fe}(\text{AgO}_4)_2$ ($R3m$, #30), and $\text{KV}_2\text{Fe}(\text{AgO}_4)_2$ ($P\bar{3}$, #31) [43–47]. These compounds also carry sizable ordered moments (as indicated by the data-point color scale). By contrast, Ga_2NiS_4 ($P\bar{3}m1$, #2) is highly frustrated with only short-range correlations; although its exact ground state and the values of its competing exchange interactions remain debated, there seems to be broad consensus that third-neighbor coupling dominates, with much weaker second-neighbor exchanges [48–53]. This is consistent with our results (see Fig. 2(a)).

For several other cases, the available experimental information remains insufficient. For instance, no magnetic measurements have been reported for TiBr_2 ($P\bar{3}m1$, #8), YCrTeO_6 ($P\bar{3}1c$, #20), $\text{KCrH}_{18}\text{N}_6(\text{ClO}_2)_4$ ($R\bar{3}$, #22), and $\text{KCrH}_{18}\text{N}_6(\text{ClO}_2)_4$ ($R\bar{3}m$, #23). In the case of MnCl_2 ($R\bar{3}m$, #6), previously reported experimental results appear inconsistent, likely due to its chemical instability and possible intercalation effects [54, 55].

Importantly, the result of synthesized materials reinforces the validity of our workflow. This observation is consistent with previous theoretical predictions and indicates that our approach effectively identifies frustrated magnetic systems. We therefore proceed to the list of unsynthesized candidates, indicated in blue in Fig. 2(a). Most of these materials are well below the critical boundary, i.e., $J_2/J_1 \lesssim 0.08$, which signals the destabilization of 120° magnetic order [29–34, 36]. The only exception is KMgNiO_6 ($P312$, #12).

	KMgNiO ₆ mp-2222843	Li ₄ Fe ₃ WO ₈ mp-756528	Li ₂ V ₃ F ₈ mp-778241	Li ₅ VP ₂ (O ₄ F) ₂ mp-758318	Li ₂ MgCo ₃ O ₈ mp-1277613	Li ₂ MgCo ₃ O ₈ mp-1177928
Lattice	Triangle (#12)	kagome (#2)	kagome (#5)	kagome (#6)	kagome (#14)	kagome (#15)
Space group	<i>P</i> 312	<i>R</i> $\bar{3}$ <i>m</i>	<i>R</i> $\bar{3}$ <i>m</i>	<i>P</i> 3	<i>P</i> 2/ <i>m</i>	<i>C</i> 2/ <i>m</i>
J_1 (meV)	0.079	0.653	0.922	0.036	2.592	2.737
J_2/J_1	0.154	0.013	0.000	0.000	0.112	0.123
$J_{3(a)}/J_1$	0.023	0.004	-0.002	-0.045	0.114	0.098
J_{3d}/J_1	-	0.454	0.000	-0.002	-0.001	0.001
J^{out}/J_1	0.008	0.003	-0.001	-0.063	0.031	0.001
m (μ_B /TM)	1.6	3.80	3.11	2.21	1.28	1.19
Predicted ground state	Stripy/120°	cuboc-1	CSL	valence-bond	$q = 0$ /cuboc-3	$q = 0$ /cuboc-3

TABLE I. Summary of six newly identified candidate magnetic materials, their crystallographic lattices, exchange-interaction parameters, and the theoretically predicted magnetic ground states. The first row lists the corresponding Materials Project identifiers (mp-IDs). The dominant exchange coupling J_1 (in meV) and its ratios with further-neighbor and interlayer couplings (J_2/J_1 , $J_{3(a)}/J_1$, J_{3d}/J_1 , and J^{out}/J_1) are obtained from first principles calculation and magnetic force theory. For kagome systems, $J_{3(a)}$ and J_{3d} correspond to the two distinct in-plane third-neighbor exchanges respectively, as marked in Fig.1(c). The ordered magnetic moment per transition-metal (TM) ion, m , is listed in units of μ_B . The last row indicates the predicted ground-state spin configuration, including noncollinear orders such as stripy and 120° states in the triangular lattice, as well as noncoplanar cuboc-1 and cuboc-3 orders and classical spin liquid (CSL) states in the kagome case. The TM species carrying local magnetic moments are indicated in bold.

KMgNiO₆ (*P*312, #12) — The detailed descriptions of its electronic structure, crystal symmetry and magnetic couplings are given in Appendix (Fig. 4 and Table IV). Importantly, this material lies close to the phase boundary between stripy and 120° order in spin-1 $J_1 - J_2$ Heisenberg model [28, 29, 35]. Our MFT calculations yield a ratio of $J_2/J_1 = 0.154$, with a small enough J_3 , as shown in Fig. 2(a). Being near the phase boundary, with $J_2/J_1 \approx 0.13$ (see also Appendix, Table IV), the system may host an intriguing magnetic phase, such as a stripy order beyond the conventional 120° state [120].

B. Catalog of kagome materials

The final list of 16 kagome compounds exhibit insulating gaps and localized spin moments at the transition-metal sites with dominant antiferromagnetic couplings ($J_1 > 0$). They are presented in Fig. 2(b), where the 9 experimentally synthesized and 7 unsynthesized materials are distinguished.

First, we examine whether the proposed workflow reproduces the well-established kagome compounds known to host frustrated magnetism, including prominent QSL candidates. Previous theoretical studies have indicated that the characteristic regime of interest satisfies $J_2/J_1 \ll 1$ and $J_{3a}, J_{3d} \ll J_1$ [37, 39–42]. Encouragingly, our screening procedure successfully recovers several benchmark systems within this regime. For example, Herbertsmithite ($\text{ZnCu}_3\text{H}_6(\text{ClO}_3)_2$, *R* $\bar{3}$ *m*, #3) [57–59] and Volborthite ($\text{V}_2\text{Cu}_3\text{H}_6\text{O}_{11}$, *C*2/*m*, #16) [60, 61] both exhibit second- and third-neighbor exchanges (J_2 , J_{3a} , J_{3d}) smaller than 10% of J_1 . A structurally related phase, $\text{V}_2\text{Cu}_3\text{H}_6\text{O}_{11}$ (*C*2, #10), differs from Volborthite only by slight lattice distortions, and our calculated exchange ratios closely reproduce those of Volborthite, suggesting a compara-

ble QSL-like behavior, although no magnetic measurements have yet been reported. Similarly, Kapellasite ($\text{ZnCu}_3\text{H}_6(\text{ClO}_3)_2$, *P* $\bar{3}$ *m*1, #1) [62, 63] yields exchange parameters in good agreement with Herbertsmithite and previous theoretical results [64–66]. Collectively, these findings demonstrate the robustness of our screening workflow described in Sec. II and its consistency with established theoretical expectations for kagome quantum spin liquids [37, 39–42].

Beyond these four benchmarks, five additional already-synthesized materials also pass our screening and exhibit exchange hierarchies indicative of strong frustration: $\text{Na}_2\text{Ti}_3\text{Cl}_8$ (*R* $\bar{3}$ *m*, #7)[121], $\text{Na}_2\text{Mn}_3\text{Cl}_8$ (*R* $\bar{3}$ *m*, #8)[122], $\text{Cs}_2\text{ZrCu}_3\text{F}_{12}$ (*R* $\bar{3}$ *m*, #11)[123], $\text{Cs}_2\text{Cu}_3\text{SnF}_{12}$ (*R* $\bar{3}$ *m*, #12) [124], and $\text{BaV}_2\text{Ni}_3(\text{HO}_5)_2$ (*C*2/*m*, #13) [125] For more quantitative fidelity, however, one typically must go beyond the minimal $J_1 - J_2 - J_3$ Heisenberg mapping to include magnetoelastic couplings, non-Heisenberg interactions (e.g., biquadratic terms), dipolar interactions, and structural distortions.

We now focus on the unsynthesized candidates (blue labels in Fig.2(b)). As described above, the final validation checks exclude $\text{Li}_2\text{Mn}_3\text{F}_8$ (*P*6₃*mc*, #4) and $\text{Li}_2\text{Nb}_3\text{Fe}_3\text{O}_8$ (*P*6₃*mc*, #9). The remaining five materials exhibit several noteworthy features summarized below:

Li₅VP₂(O₄F)₂ (*P*3, #6) — The detailed descriptions of its electronic structure, crystal symmetry and magnetic couplings are given in Fig. 5 and Table V. A notable feature of this material is the small J_1 and the even smaller further-neighbor couplings. As shown in Fig. 2(b) and Table I, J_2/J_1 and $J_{3d}/J_1 \approx 0$, while J_{3a} is also less than 5% of J_1 . This hierarchy is robust across an alternative DFT+*U* functional and nine combinations of (*U*, *J_H*) (Appendix, Table V). It is therefore suggested that $\text{Li}_5\text{VP}_2(\text{O}_4\text{F})_2$ is a promising candidate for the

valence-bond type order proposed for spin-1 systems [72].

Li₂V₃F₈ (*R* $\bar{3}m$, #5) — Our exchange mapping yields a dominant $J_1 = 0.922$ meV, while J_2 , J_{3a} and J_{3d} are negligible (Fig. 2(b) and Table I). This exchange hierarchy is robust across alternative DFT+ U functionals and multiple (U, J_H) choices (Appendix, Table VI), placing Li₂V₃F₈ in the J_1 -only regime of the kagome Heisenberg model. In this sense, it closely resembles Li₅VP₂(O₄F)₂. Owing to its larger spin magnitude ($S = 3/2$), however, Li₂V₃F₈ approaches the classical limit of the kagome antiferromagnet, where strong frustration gives rise to a classical spin liquid (CSL) manifold. The corresponding crystal and electronic structures are shown in Appendix, Fig. 6.

Li₄Fe₃WO₈ (*R* $\bar{3}m$, #2) — The calculated first-neighbor $J_1 = 0.653$ meV with the corresponding interatomic Fe–Fe distance is 3.09 Å (Table I and Fig. 7). A particularly notable feature of this compound is the exceptionally large across-hexagon third-neighbor coupling J_{3d} , which exceeds 45% of J_1 , and is larger than both J_2 and J_{3a} (Fig. 2(b) and Table I). This unusually strong interaction is attributed to superexchange pathways mediated by the central W⁶⁺ ions, located at the centers of the hexagonal plaquettes (Appendix, Fig. 7). This hierarchy is robust to the choice of DFT+ U functional and on-site parameters: across all calculations we obtain $J_{3d}/J_1 \geq 0.147$ (Appendix, Table VII). A comparably large J_{3d} competing with J_1 is known to stabilize exotic non-coplanar states, namely ‘cuboc-1’ phase (Table I).

Li₂MgCo₃O₈ (*P*2/ m , #14) & Li₂MgCo₃O₈ (*C*2/ m , #15) — These two sister compounds are quite similar except for a slight distortion: the Co–Co distances agree to within ~ 0.1 Å, and the exchange couplings differ by less than 0.1 meV (Table I and Appendix). A notable feature in this family is the magnitude of J_2 and J_{3a} : their J_2/J_1 and J_{3a}/J_1 values are largest in Fig. 2(b). This unusual interaction profile has important consequences. Even in the classical limit they point to a nontrivial magnetic order; based on the specific exchange hierarchy, we tentatively refer to the anticipated state as ‘cuboc-3’, distinct from the previously-reported cuboc-1 and cuboc-2 phases on the kagome lattice [73]. Moreover, given the effective spin moment of $S \approx 1/2$, strong quantum fluctuations are expected to play a significant role, suggesting a possible link to chiral quantum spin liquid behavior. Broader implications for the resulting frustrated magnetism are further discussed below.

To summarize, mapping the exchange hierarchies of the five kagome-lattice candidates onto the classical J_1 – J_2 – J_{3a} – J_{3d} phase space reveals a rich landscape of magnetic behavior (see below). The J_1 -dominated compounds, such as Li₅VP₂(O₄F)₂ and Li₂V₃F₈, are ex-

pected to host CSL or valence-bond type order in the absence of magnetic Bragg peaks. In contrast, compounds such as Li₄Fe₃WO₈ and Li₂MgCo₃O₈ exhibit stronger further-neighbor couplings: the across-hexagon interaction J_{3d} stabilizes noncoplanar cuboc-1 order characterized by a 2×2 magnetic superstructure, while competition between the along-bond third-neighbor J_{3a} and J_2 interactions gives rise to a previously unreported cuboc-3 phase with an even larger real-space periodicity and a distinct reciprocal-space signature.

C. Classical spin phase diagram on the kagome lattice

Using the suggested workflow, we identified one triangular lattice and five kagome lattice candidates that have not yet been synthesized and are expected to host nontrivial magnetic phases. Notably, several kagome candidates exhibit sizable further-neighbor couplings in addition to the NN exchange. The kagome J_1 – J_2 – J_{3d} Heisenberg model has been extensively studied in both classical and quantum regimes: classically it supports noncoplanar orders such as cuboc-1 and cuboc-2, while for $S = \frac{1}{2}$ it admits spin-liquid regimes (e.g., $U(1)$ and Z_2) and, for appreciable J_2 or J_{3d} , chiral spin-liquid phases [100–107]. While the along-bond 3rd NN coupling J_{3a} has also been studied, most prior work has concentrated on the special line $J_2 = J_{3a}$ case [108–116].

In contrast, the generic case $J_2 \neq J_{3a}$, relevant to our materials, remains comparatively unexplored. Accordingly, we analyze the full J_1 – J_2 – $J_{3a(3d)}$ model relevant to our materials and show how a finite J_{3a} reshapes the phase competition, potentially stabilizing new magnetic orders. The Hamiltonian is given by

$$\mathcal{H} = J_1 \sum_{\langle i,j \rangle} \vec{S}_i \cdot \vec{S}_j + J_2 \sum_{\langle\langle i,j \rangle\rangle} \vec{S}_i \cdot \vec{S}_j + J_{3a(3d)} \sum_{\langle\langle\langle i,j \rangle\rangle\rangle} \vec{S}_i \cdot \vec{S}_j. \quad (2)$$

Here, J_1 , J_2 , and J_{3a} (J_{3d}) represent the antiferromagnetic Heisenberg interaction strengths for the first, second, and third NNs along the bonds (across the hexagonal plaquettes), respectively (see Fig.1(c)).

Fig. 3(a) and (b) present the classical phase diagrams for the J_1 – J_2 – J_{3d} and J_1 – J_2 – J_{3a} models on the kagome lattice, using the Luttinger–Tisza method and the Landau–Lifshitz–Gilbert equation. In each phase diagram, we found various classical spin orderings: the $q = 0$ phase, the sublattice antiferromagnetic phase, the $\sqrt{3} \times \sqrt{3}$ phase, and several types of cuboctahedral phases.

q = 0 phase — The first and second NN Heisenberg interactions on the kagome lattice can be rewritten in

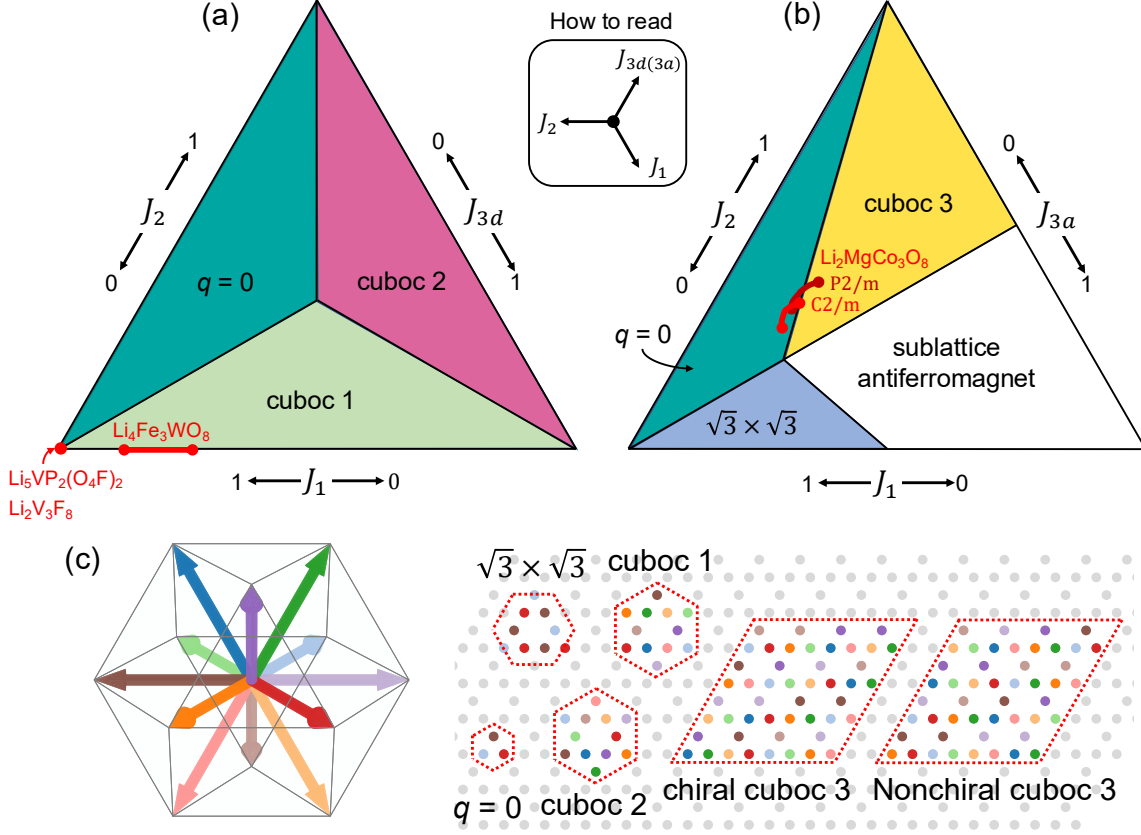


FIG. 3. Classical ternary phase diagrams for (a) $J_1 - J_2 - J_{3d}$ and (b) $J_1 - J_2 - J_{3a}$ kagome Heisenberg models. Couplings are normalized such that $J_1 + J_2 + J_{3a(3d)} = 1$. The dashed region indicates the parameter regime of the material obtained from the DFT+ U calculation. The inset illustrates how to read the ternary phase diagram. (c) Real-space spin configurations for each ordered phase. The spin colors correspond to the spin directions on the cuboctahedron shown on the left.

terms of the sum of spins on triangular plaquettes as

$$\mathcal{H}_{1,2} = J_{1,2} \sum_{ijk} \left(\vec{S}_i + \vec{S}_j + \vec{S}_k \right)^2 - (\text{const.}), \quad (3)$$

where ijk denotes sets of three spins forming the small (for J_1) and large (for J_2) triangles of the kagome lattice. This form clearly indicates that energy is minimized when the spins on each triangle form a coplanar 120° configuration, satisfying $\vec{S}_i + \vec{S}_j + \vec{S}_k = \vec{0}$. As both J_1 and J_2 terms independently favor this spin arrangement, the system naturally realizes a uniform 120° ordering on all small and large triangular plaquettes. The resulting spin configuration is characterized by a wave vector $\vec{q} = \vec{0}$, where each magnetic unit cell coincides with the original unit cell (see Fig. 3(c)). This ordered state is referred to as the $q = 0$ phase.

Sublattice Antiferromagnet — In the $J_1 - J_2 - J_{3a}$ model, J_{3a} connects spins on the same sublattice across adjacent unit cells. In the limit of dominant J_{3a} , the kagome lattice effectively decomposes into three decoupled NN

antiferromagnetic Heisenberg models defined on square lattices. In this limit, the energy is minimized when each sublattice independently forms a Néel order, and the relative spin orientations between different sublattices become energetically irrelevant. This magnetic order pattern is referred to as the sublattice antiferromagnet phase.

$\sqrt{3} \times \sqrt{3}$ phase — Among the degenerate classical ground states of the pure J_1 Heisenberg model on the kagome lattice, where the spins on each triangle satisfy the constraint $\vec{S}_i + \vec{S}_j + \vec{S}_k = \vec{0}$, the inclusion of further-neighbor interactions can lift the degeneracy and select a specific spin configuration. In the case of dominant J_{3a} term compare to J_2 , which connects spins on the same sublattice across adjacent unit cells, the J_{3a} term favors a relative 120° spin arrangement among equivalent sublattices, effectively enlarging the magnetic unit cell. This results in a $\sqrt{3} \times \sqrt{3}$ magnetic structure, as illustrated in Fig. 3(c). We refer to this state as the $\sqrt{3} \times \sqrt{3}$ phase due to the tripling of the original unit cell area.

Cuboctahedron phases — The classical phase diagrams of the $J_1 - J_2 - J_{3d}$ and $J_1 - J_2 - J_{3a}$ models reveal three types of cuboctahedral spin orderings: cuboc-1 and cuboc-2 in the $J_1 - J_2 - J_{3d}$ model [101, 105, 117, 118], and a novel cuboc-3 phase in the $J_1 - J_2 - J_{3a}$ model, as shown in Fig. 3(c). While the cuboc-1 and cuboc-2 phases have been previously studied, the cuboc-3 phase emerges as a new classical spin configuration found in the current work. We provide a brief review cuboc-1 and cuboc-2 phases and then focus on a detailed characterization of the newly identified cuboc-3.

Cuboc-1 : For antiferromagnetic J_1 , the NN Heisenberg term enforces the local constraint $\vec{S}_i + \vec{S}_j + \vec{S}_k = \vec{0}$ on every primitive (up/down) triangle, which is satisfied by coplanar 120° configurations. Introducing an across-hexagon third-neighbor coupling J_{3d} selects, out of this manifold, a noncoplanar twelve-sublattice state, the cuboc-1 order. In this phase, the magnetic unit cell enlarges to 2×2 times the kagome unit cell (12 spins), with spin directions pointing to the 12 vertices of a cuboctahedron (see Fig. 3(c)). While each small J_1 triangle remains 120° to minimize the NN energy, neighboring triangles are rotated out of a common plane so that certain larger triangles acquire a finite scalar chirality, $\vec{S}_i \cdot (\vec{S}_j \times \vec{S}_k) \neq 0$.

Cuboc-2 : Using a similar analogy to the cuboc-1 phase, J_2 prefers 120° spin ordering to minimize the 2nd NN triangular plaquettes. When J_{3d} is introduced, each 2nd NN spin configuration preserves a coplanar 120° spin order, but the primitive triangular plaquettes become non-coplanar. Therefore, in contrast to the cuboc-1 phase, the primitive triangular plaquettes exhibit a non-zero scalar spin chirality, $\vec{S}_i \cdot (\vec{S}_j \times \vec{S}_k) \neq 0$ for $J_2 - J_{3d}$ model. Nevertheless, the global spin configuration still places each spin direction on the vertices of a cuboctahedron, forming an enlarged 2×2 magnetic unit cell similar to cuboc-1 (see Fig. 3(c)). To distinguish it from the cuboc-1 state, this phase is referred to as the cuboc-2 phase.

Cuboc-3 : In this study, we identify a novel type of cuboctahedral spin ordering in the $J_1 - J_2 - J_{3a}$ model on the kagome lattice. This new ordering, which we refer to as the cuboc-3 phase, emerges from the competition between the J_{3a} and J_2 interactions. While the J_{3a} term favors Néel ordering within each sublattice, the J_2 interaction stabilizes coplanar 120° configurations on the large triangles of the kagome lattice. As a result, the spin configuration simultaneously satisfies the 120° coplanar condition on all large triangles and realizes antiferromagnetic order within each 2×2 sublattice. This leads to an enlarged magnetic unit cell of 4×4 relative to the original kagome unit cell (see Fig. 3(c)). The spin directions align with the vertices of a cuboctahedron, but in a pattern

distinct from the previously known cuboc-1 and cuboc-2 phases.

Interestingly, the cuboc-3 phase exhibits twofold degeneracy: a chiral and a non-chiral configuration. In the chiral cuboc-3 state, the scalar spin chirality $\vec{S}_i \cdot (\vec{S}_j \times \vec{S}_k)$ is finite on each up and down small triangle plaquette. In contrast, the non-chiral configuration maintains coplanar spin order on all small and large triangles, resulting in vanishing scalar spin chirality, $\vec{S}_i \cdot (\vec{S}_j \times \vec{S}_k) = 0$, as shown in Fig. 3(c).

In the phase diagram shown in Fig. 3(a) and (b), we indicate the parameter regimes corresponding to each kagome material candidate using red lines. It is noted that $\text{Li}_5\text{VF}_2(\text{O}_4\text{F})_2$ and $\text{Li}_2\text{V}_3\text{F}_8$ are located in the regime dominated by the NN interaction, effectively corresponding to the pure J_1 Heisenberg model (see Fig. 3(a)). Its classical ground states form an extensively degenerate manifold, known as the Coulomb spin liquid phase [119]. These materials therefore provide the promising platforms to explore highly frustrated classical spin-liquid physics.

Next, $\text{Li}_4\text{Fe}_3\text{WO}_8$ lies within the cuboc-1 stability region, having comparable J_1 and J_{3d} (see Fig. 3(a)). This positioning in parameter space highlights $\text{Li}_4\text{Fe}_3\text{WO}_8$ as a compelling platform for investigating kagome noncoplanar order and motivates the targeted experimental verification of the predicted cuboc-1 pattern.

Finally, $\text{Li}_2\text{MgCo}_3\text{O}_8$ falls into a parameter regime where multiple phases, such as cuboc-3 and $q = 0$, can potentially emerge (see Fig. 3(b)). The precise ground state depends sensitively on microscopic parameters, including the strength of Hund's coupling and on-site Coulomb interactions. In the quantum regime, only the special case with $J_2 = J_{3a}$ has been studied so far [108, 111, 116]. This highlights $\text{Li}_2\text{MgCo}_3\text{O}_8$ as not only an intriguing material candidate for realizing exotic magnetic orders but also as a promising platform for exploring quantum phases in the $J_1 - J_2 - J_{3a}$ model. Further investigation of this model in the quantum regime thus represents an important direction for future work

IV. COMPUTATION DETAILS

DFT+ U calculations were performed using the OpenMX package [84], which employs a localized pseudoatomic orbital basis set. For the exchange–correlation functional, we adopted the generalized gradient approximation (GGA) [85], with a cutoff energy of 700 Ry and a \mathbf{k} -point mesh denser than 0.18 \AA^{-1} . As described above, we used the DFT+ U_{eff} method [86, 87] at the first stage (the third screening step), with U_{eff} values taken from Ref. [88]. Additional checks of the dependence on the choice of DFT+ U functional, double-counting formalism as well as on the Hubbard U and Hund's J_H , were performed at later stages (the sixth step). To verify the robustness of our results, additional computations were conducted with an alternative functional formalism [89, 99], DFT spin-part control [91–93, 99] and varying the in-

teraction parameters in a $\sim 10\%$ range. As mentioned above, two kagome candidate materials were excluded in this final validity check stage. For $\text{Li}_2\text{Mn}_3\text{F}_8$, charge-only DFT (cDFT) with the rotationally invariant Liechtenstein $+U + J_H$ scheme yields a ferromagnetic J_1 , in contrast to the spin-polarized GGA/LDA+ U mapping. Similar sensitivities to the functional choice (charge-only vs spin-polarized) have been reported for CrOCl , CrOBr , and LaMnO_3 [94, 95]. For $\text{Li}_2\text{Nb}_3\text{Fe}_3\text{O}_8$, the Liechtenstein cDFT+ $U + J_H$ and Dudarev implementation agree only in the large- U limit; at small U they predict different ordered moments and opposite signs for the leading exchange coupling.

For MFT calculations, ‘Jx’ code is used [96, 97]. Full-band spin-dependent Kohn-Sham Hamiltonian taken from DFT+ U calculations serves as the input for MFT after the proper symmetrization process to improve the accuracy. The estimation of Eq.(1) in the manuscript comes through

$$[\mathbf{G}_{\mathbf{k},ij}]_{l_1 l_2}^\sigma = \sum_n \frac{|w_{l_1, \mathbf{k}, i}^\sigma \langle w_{l_2, \mathbf{k}, j}^\sigma |}{z - \epsilon_{\sigma, n, \mathbf{k}} + i0^+}, \quad (4)$$

where $\sigma = \uparrow, \downarrow$ are spin indices, and the orbital l_1 and l_2 belong to the atomic site i and j , respectively. $|w_{l_1, \mathbf{k}, i}^\sigma\rangle$ refers to the local state. The final real-space value is obtained through Fourier transformation,

$$J(\mathbf{R}_{ij}) = \sum_{l_1 l_2} \tilde{J}^{l_1 l_2}(\mathbf{R}_{ij}) = \sum_{l_1 l_2} \sum_{\mathbf{q}} \tilde{J}_{ij}^{l_1 l_2}(\mathbf{q}) e^{-i\mathbf{R}_{ij} \cdot \mathbf{q}}. \quad (5)$$

At the earlier screening stage, magnetic couplings are estimated based on the ferromagnetic order for convenience, as it is expected to give a reasonable value for well-localized moments, which should be the case of our interest [96–98]. Eventually, this estimation is double-checked with the antiferromagnetic solution. We first take as many \mathbf{q} -points as in the \mathbf{k} -points mesh of the DFT calculations. After screening out, we double-check the candidate materials with a denser mesh whose largest grid spacing is less than 0.15 \AA^{-1} , and with optimized basis functions.

V. CONCLUSION AND DISCUSSION

We developed a targeted workflow for discovering frustrated magnets by integrating high-throughput first-principles calculations, magnetic-force theory, and spin-Hamiltonian analysis. Screening nearly 150,000 compounds, the framework identifies $3d$ kagome and triangular systems, reproduces known benchmarks, and reveals previously unexplored candidates with quantitatively resolved further-neighbor exchanges. By connecting large-scale electronic-structure data to model-level descriptions, it

provides a predictive and physically transparent route from ab initio calculations to emergent magnetic behavior.

This approach demonstrates how high-throughput materials discovery can be made both selective and interpretable by focusing on motifs of magnetic frustration. The framework is readily extensible to include symmetry-based anisotropy diagnostics, uncertainty quantification, and machine-learning acceleration, and can be generalized to other frustrated lattices such as breathing or hyperkagome networks and to tunable parameters including pressure, epitaxial strain, and chemical substitution.

Because several relevant exchanges are in the sub-meV range, small perturbations beyond the bilinear Heisenberg form such as Dzyaloshinskii–Moriya anisotropy, bi-quadratic and ring exchanges, and magnetoelastic couplings, may become decisive near phase boundaries. While our calculations confirm the robustness of the dominant exchange hierarchy, a comprehensive treatment of spin-orbit induced anisotropies and quantum-fluctuation effects represents a natural next step for future work.

VI. ACKNOWLEDGEMENTS

B. H. J. and H. S. K. contributed equally to this work. We thank Minu Kim, Jaewook Kim, and Jongmok Ok for valuable discussions on the possibility of experimental synthesis. B. H. J. and M. J. H. are grateful to Jiwon Kim for helpful support in data verification. This work was supported by the National Research Foundation of Korea (NRF) grant funded by the Korean government (MSIT) (Grant Nos. RS-2025-02243032 and RS-2025-00559042).

VII. DATA AVAILABILITY

The data that support the findings of this study are available from the corresponding author upon reasonable request.

VIII. APPENDIX

- A. The detailed information of 32 triangular and 16 kagome materials (Table II and III)
- B. Crystal and electronic structure of six new materials (Fig. 4–9)
- C. The exchange couplings for six new materials calculated within charge-DFT plus U and J_H functional (Table IV–IX)

[1] Anderson, P. W. Resonating valence bonds: A new kind of insulator? *Mater. Res. Bull.* **8**, 153–160 (1973).

[2] Savary, L. & Balents, L. Quantum spin liquids: a review. *Rep. Prog. Phys.* **80**, 016502 (2016).

number	mp-id	Formula	S.G.	m/TM (μ_B)	J_1^{avg} (meV)	J_1^{STD}	$J_2^{\text{avg}}/J_1^{\text{avg}}$	$J_3^{\text{avg}}/J_1^{\text{avg}}$
1	mp-754490	NiHgO ₂	$R\bar{3}$	1.63	3.06	0.04	0.01	0.22
2	mp-6959	Ga ₂ NiS ₄	$P\bar{3}m1$	1.37	5.77	0.02	0.01	0.22
3	mp-625939	Co(HO) ₂	$C2$	2.74	0.46	0.10	0.00	0.12
4	mp-22877	VCl ₂	$P\bar{3}m1$	3.19	0.13	0.00	0.03	0.13
5	mp-2665409	Co(HO) ₂	$C2/m$	2.74	0.55	0.09	0.00	0.07
6	mp-28233	MnCl ₂	$R\bar{3}$	4.93	0.04	0.00	0.05	0.12
7	mp-1207060	TiI ₂	$P\bar{3}m1$	2.26	1.02	0.01	0.05	0.06
8	mp-27785	TiBr ₂	$P\bar{3}m1$	2.15	0.44	0.01	0.07	0.07
9	mp-28116	TiCl ₂	$P\bar{3}m1$	2.07	1.73	0.01	0.03	0.01
10	mp-1228485	Al ₃ CrO ₆	$R\bar{3}$	3.16	0.04	0.00	0.04	0.00
11	mp-2210657	MgTiO ₂	$R\bar{3}$	2.03	15.13	0.12	0.01	-0.04
12	mp-2222843	KMgNiO ₆	$P312$	1.6	0.08	0.00	0.15	0.02
13	mp-625671	Mn(HO) ₂	$P1$	4.94	0.12	0.01	0.00	0.05
14	mp-2217116	MgMn(CO ₃) ₂	$R\bar{3}$	4.96	0.02	0.00	0.00	0.04
15	mp-1078415	CaFeSO	$P6_3mc$	3.76	0.73	0.14	0.01	0.04
16	mp-2210666	MgMnO ₂	$R3m$	4.85	0.64	0.00	0.00	0.02
17	mp-755288	LiFeCuS ₂	$P3m1$	3.73	1.26	0.21	0.01	0.02
18	mp-1222418	NaFeCuS ₂	$P3m1$	3.72	1.20	0.20	0.01	0.02
19	mp-1208041	TlCr(SO ₄) ₂	$P321$	3.23	0.02	0.00	0.01	0.03
20	mp-1105234	YCrTeO ₆	$P\bar{3}1c$	3.13	0.15	0.00	0.00	0.00
21	mp-1177936	Li ₂ Mn(SeO ₃) ₂	$R\bar{3}$	4.93	0.06	0.00	0.00	0.00
22	mp-24100	KCrH ₁₈ N ₆ (ClO ₂) ₄	$R\bar{3}$	3.47	0.00	0.00	0.00	0.00
23	mp-24099	KCrH ₁₈ N ₆ (ClO ₂) ₄	$R\bar{3}m$	3.47	0.00	0.00	0.00	0.00
24	mp-1209246	RbCr(SO ₄) ₂	$P321$	3.11	0.22	0.00	0.00	0.00
25	mp-1214516	Ba ₃ Nb ₂ NiO ₉	$P\bar{3}m1$	1.65	0.17	0.00	0.00	0.00
26	mp-684724	FeH ₄ S ₂ NO ₈	$R\bar{3}$	4.15	0.32	0.00	0.00	0.00
27	mp-560628	CsFe(SO ₄) ₂	$P\bar{3}$	4.14	0.34	0.00	0.00	-0.01
28	mp-1218186	SrMnTeO ₆	$P\bar{6}$	3.64	0.18	0.00	0.01	0.01
29	mp-1213686	CsCr(MoO ₄) ₂	$P\bar{3}m1$	2.99	0.17	0.00	0.02	0.01
30	mp-1103452	RbV ₂ Fe(AgO ₄) ₂	$P\bar{3}$	4.06	0.23	0.00	0.01	0.00
31	mp-1103811	KV ₂ Fe(AgO ₄) ₂	$P\bar{3}$	4.05	0.23	0.00	0.01	0.00
32	mp-1227585	CaTi ₈ Mn(PO ₄) ₁₂	$R\bar{3}$	5.02	0.00	0.00	0.01	0.00

TABLE II. The calculation results of 32 triangular materials listed in Fig.2(a): magnetic moments at transition-metal sites, J_1^{avg} , the standard deviation of J_1 , $J_2^{\text{avg}}/J_1^{\text{avg}}$, and $J_3^{\text{avg}}/J_1^{\text{avg}}$.

number	mp-id	Formula	S.G.	m/TM (μ_B)	J_1^{avg} (meV)	J_1^{STD}	$J_2^{\text{avg}}/J_1^{\text{avg}}$	$J_{3a}^{\text{avg}}/J_1^{\text{avg}}$	$J_{3d}^{\text{avg}}/J_1^{\text{avg}}$
1	mp-560161	ZnCu ₃ H ₆ (ClO ₃) ₂	$P\bar{3}m1$	0.48	21.33	0.01	-0.05	0.02	0.40
2	mp-756528	Li ₄ Fe ₃ WO ₈	$R\bar{3}m$	3.80	0.65	0.00	0.01	0.00	0.45
3	mp-1189352	ZnCu ₃ H ₆ (ClO ₃) ₂	$R\bar{3}m$	0.48	116.49	0.00	-0.08	-0.04	0.02
4	mp-763793	Li ₂ Mn ₃ F ₈	$P6_3mc$	4.99	0.08	0.04	0.00	0.01	0.00
5	mp-778241	Li ₂ V ₃ F ₈	$R\bar{3}m$	3.11	0.92	0.00	0.00	0.00	0.00
6	mp-758318	Li ₅ VP ₂ (O ₄ F) ₂	$P3$	2.21	0.04	0.00	0.00	-0.04	0.00
7	mp-29474	Na ₂ Ti ₃ Cl ₈	$R\bar{3}m$	2.09	0.10	0.00	0.02	0.08	0.08
8	mp-27126	Na ₂ Mn ₃ Cl ₈	$R\bar{3}m$	4.93	0.03	0.00	0.03	0.16	0.09
9	mp-775011	Li ₂ NbFe ₃ O ₈	$P6_3mc$	4.08	2.27	1.82	0.03	0.01	0.00
10	mp-1216869	V ₂ Cu ₃ H ₆ O ₁₁	$C2$	0.56	78.59	15.67	0.03	0.00	-0.01
11	mp-9202	Cs ₂ ZrCu ₃ F ₁₂	$R\bar{3}m$	0.73	26.42	0.00	0.05	-0.04	-0.01
12	mp-1106088	Cs ₂ Cu ₃ SnF ₁₂	$R\bar{3}m$	0.72	21.81	0.00	0.05	-0.03	-0.01
13	mp-1205427	BaV ₂ Ni ₃ (HO ₅) ₂	$C2/m$	1.64	2.39	0.06	0.09	0.08	0.01
14	mp-1277613	Li ₂ MgCo ₃ O ₈	$P2/m$	1.28	2.59	0.58	0.11	0.11	0.01
15	mp-1177928	Li ₂ MgCo ₃ O ₈	$C2/m$	1.19	2.77	0.54	0.12	0.10	0.00
16	mp-721062	V ₂ Cu ₃ H ₆ O ₁₁	$C2/m$	0.55	84.96	19.96	0.03	0.05	-0.10

TABLE III. The calculation results of 16 kagome materials listed in Fig.2(b): magnetic moments at transition-metal sites, J_1^{avg} , the standard deviation of J_1 , $J_2^{\text{avg}}/J_1^{\text{avg}}$, $J_{3a}^{\text{avg}}/J_1^{\text{avg}}$, and $J_{3d}^{\text{avg}}/J_1^{\text{avg}}$.

- [3] Zhou, Y., Kanoda, K. & Ng, T.-K. Quantum spin liquid states. *Rev. Mod. Phys.* **89**, 025003 (2017).
- [4] Wen, X.-G. Colloquium: Zoo of quantum-topological phases of matter. *Rev. Mod. Phys.* **89**, 041004 (2017).
- [5] Broholm, C. *et al.* Quantum spin liquids. *Science* **367**, eaay0668 (2020).
- [6] Norman, M. Colloquium: Herbertsmithite and the search for the quantum spin liquid. *Rev. Mod. Phys.* **88**, 041002 (2016).
- [7] Mounet, N. *et al.* Two-dimensional materials from high-throughput computational exfoliation of experimentally known compounds. *Nat. Nanotechnol.* **13**, 246–252 (2018).

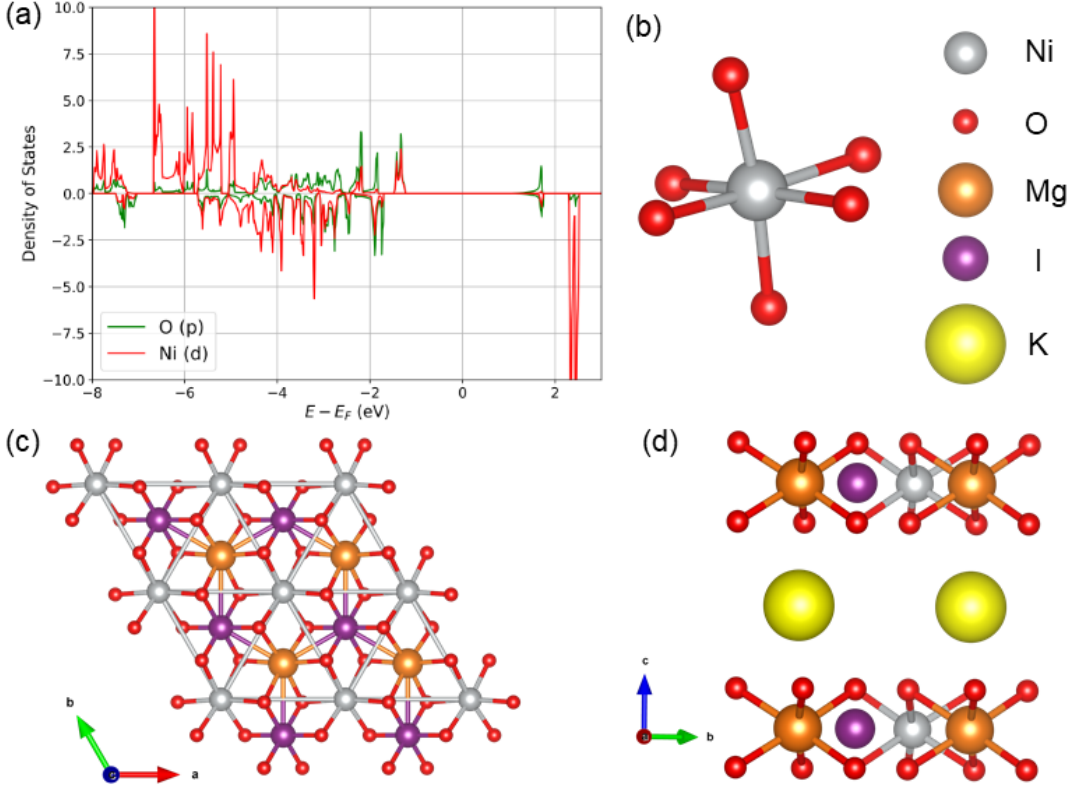


FIG. 4. (a) Projected density of states (PDOS) for KMgNiO_6 ($P312$). The red and green lines represent the Ni-3d and O-2p states (per atom), respectively. (b) The local atomic structure around transition-metal site (NiO_6). (c) Top and (d) side view of the crystal structure. The Ni^{2+} ions in the NiO_6 octahedral environment adopt a $t_{2g}^6 e_g^2$ electronic configuration. Each triangular Ni layer is well isolated by non-magnetic K layers, resulting in a quasi-two-dimensional magnetic lattice. The C_3 rotational symmetry along the (001) axis and the C_2 symmetry along the (210) direction within the triangular plane ensure that all NN exchange couplings (J_1) are equivalent. The NN Ni-Ni distance is 5.24\AA , and the magnetic superexchange pathway involves two distinct long-range bridges: Ni-O-I-O-Ni and Ni-O-Mg-O-Ni. These extended exchange paths give rise to a weak antiferromagnetic coupling with a small value of $J_1 = 0.079$ meV.

- [8] Vergniory, M. *et al.* A complete catalogue of high-quality topological materials. *Nature* **566**, 480–485 (2019).
- [9] Zhang, T. *et al.* Catalogue of topological electronic materials. *Nature* **566**, 475–479 (2019).
- [10] Tang, F., Po, H. C., Vishwanath, A. & Wan, X. Comprehensive search for topological materials using symmetry indicators. *Nature* **566**, 486–489 (2019).
- [11] Xu, Y. *et al.* High-throughput calculations of magnetic topological materials. *Nature* **586**, 702–707 (2020).
- [12] Wu, Y. *et al.* Data-driven discovery of high performance layered van der Waals piezoelectric NbOI_2 . *Nat. Commun.* **13**, 1884.
- [13] Regnault, N. *et al.* Catalogue of flat-band stoichiometric materials. *Nature* **603**, 824–828.
- [14] Gao, Z. *et al.* High-throughput screening of 2D van der Waals crystals with plastic deformability. *Nat. Commun.* **13**, 7491.
- [15] Jin, R., Yuan, X. & Gao, E. Atomic stiffness for bulk modulus prediction and high-throughput screening of ultraincompressible crystals. *Nat. Commun.* **14**, 4258.
- [16] Li, Y. *et al.* High-throughput screening and machine learning classification of van der Waals dielectrics for 2D nanoelectronics. *Nat. Commun.* **15**, 9527.
- [17] Björk, J., Zhou, J., Persson, P. O. & Rosen, J. Two-dimensional materials by large-scale computations and chemical exfoliation of layered solids. *Science* **383**, 1210–1215 (2024).
- [18] Chen, X. *et al.* Unconventional magnons in collinear magnets dictated by spin space groups. *Nature* **640**, 349–354.
- [19] Meschke, V., Gorai, P., Stevanovic, V. & Toberer, E. S. Search and structural featurization of magnetically frustrated kagome lattices. *Chem. Mater.* **33**, 4373–4381 (2021).
- [20] Hallett, A., Avarvarei, C. & Harter, J. W. Combinatorial exploration of quantum spin liquid candidates in the herbertsmithite material family. *Phys. Rev. Mater.* **7**, 064403 (2023).
- [21] Jain, A. *et al.* Commentary: The Materials Project: A materials genome approach to accelerating materials innovation. *APL Mater.* **1**, 011002 (2013).
- [22] Karigerasi, M. H., Wagner, L. K. & Shoemaker, D. P. Uncovering anisotropic magnetic phases via fast dimensionality analysis. *Phys. Rev. Mater.* **2**, 094403 (2018).
- [23] Generalic, E. Oxidation numbers calculator. https://www.periodni.com/oxidation_numbers_

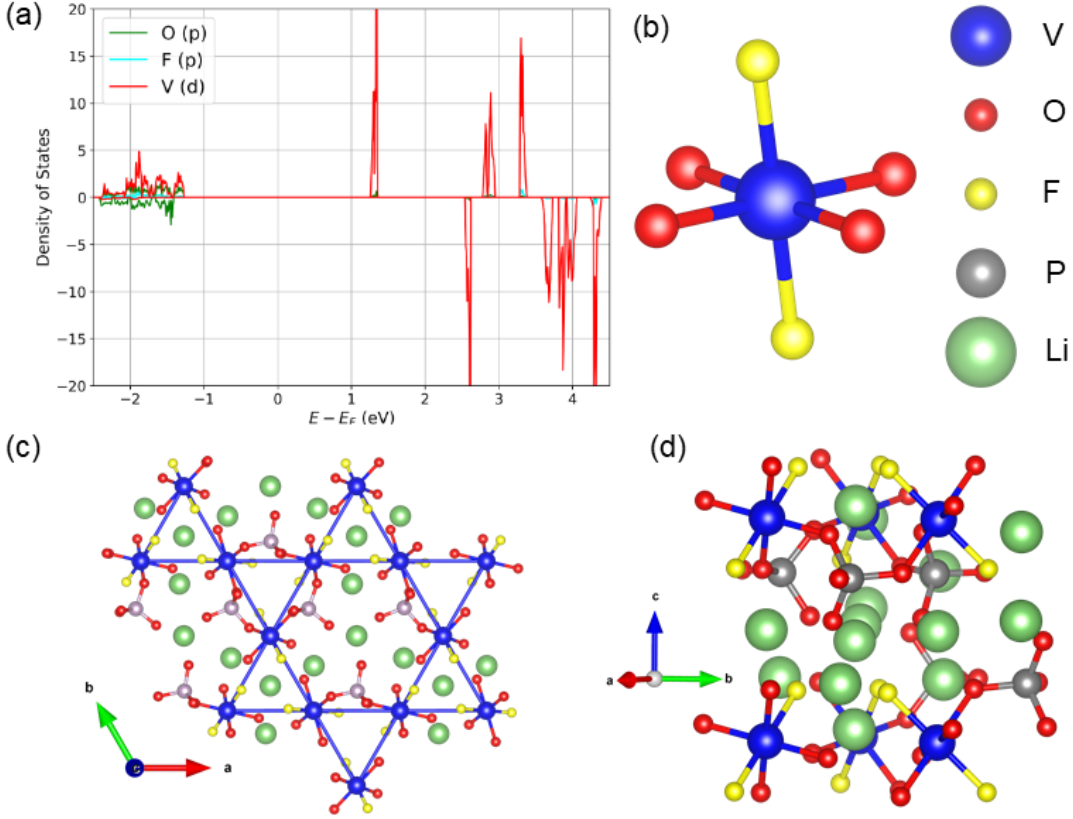


FIG. 5. (a) PDOS for $\text{Li}_5\text{VP}_2(\text{O}_4\text{F})_2(P3)$. The red, green and cyan lines represent the V-3d, O-2p and F-2p states (per atom), respectively. (b) The local atomic structure around transition-metal site (VO_4F_2). (c) Top and (d) side view of the crystal structure. The V^{3+} ions, coordinated by O_4F_2 octahedra, nominally host two valence electrons in t_{2g} orbitals. While C_3 rotational symmetry around the (001) axis is preserved, the presence of inter-layer Li ions breaks inversion symmetry, leading to a lowering of the overall lattice symmetry. As a result, the NN magnetic interactions split into two symmetry-inequivalent values, despite the underlying C_3 and translational symmetries. Consistent with this expectation, our MFT calculations yield two distinct NN couplings: $J_1 = 0.035$ and 0.036 meV. In the Supplementary Table. V, we report the average of these two values for simplicity. The long interatomic V-V distance of 5.05\AA , coupled with extended superexchange pathways (V-O-Li-F-V and V-O-Li-O-V) accounts for the relatively small magnitude of J_1 .

- calculator.php (2024). EniG. Periodic Table of the Elements. KTF-Split, Accessed: 2024-11-13.
- [24] Liechtenstein, A. I., Katsnelson, M., Antropov, V. & Gubanov, V. Local spin density functional approach to the theory of exchange interactions in ferromagnetic metals and alloys. *J. Magn. Magn. Mater.* **67**, 65–74 (1987).
- [25] Antropov, V., Katsnelson, M., Harmon, B., Van Schilf-gaarde, M. & Kusnezov, D. Spin dynamics in magnets: Equation of motion and finite temperature effects. *Phys. Rev. B* **54**, 1019 (1996).
- [26] Katsnelson, M. & Lichtenstein, A. First-principles calculations of magnetic interactions in correlated systems. *Phys. Rev. B* **61**, 8906 (2000).
- [27] Han, M. J., Ozaki, T. & Yu, J. Electronic structure, magnetic interactions, and the role of ligands in Mnn ($n = 4, 12$) single-molecule magnets. *Phys. Rev. B* **70**, 184421 (2004).
- [28] Rubin, P., Sherman, A. & Schreiber, M. The spin-1 two-dimensional $J_1 - J_2$ Heisenberg antiferromagnet on a triangular lattice. *Phys. Lett. A* **374**, 3567–3571 (2010).
- [29] Xu, C., Wang, F., Qi, Y., Balents, L. & Fisher, M. P. Spin liquid phases for spin-1 systems on the triangular lattice. *Phys. Rev. Lett.* **108**, 087204 (2012).
- [30] Li, P. H., Bishop, R. F. & Campbell, C. E. Quasiclassical magnetic order and its loss in a spin-1/2 Heisenberg antiferromagnet on a triangular lattice with competing bonds. *Phys. Rev. B* **91**, 014426 (2015).
- [31] Zhu, Z. & White, S. R. Spin liquid phase of the $S = 1/2$ $J_1 - J_2$ Heisenberg model on the triangular lattice. *Phys. Rev. B* **92**, 041105 (2015).
- [32] Iqbal, Y., Hu, W.-J., Thomale, R., Poilblanc, D. & Becca, F. Spin liquid nature in the Heisenberg $J_1 - J_2$ triangular antiferromagnet. *Phys. Rev. B* **93**, 144411 (2016).
- [33] Saadatmand, S. & McCulloch, I. Symmetry fractionalization in the topological phase of the spin-1/2 $J_1 - J_2$ triangular Heisenberg model. *Phys. Rev. B* **94**, 121111 (2016).
- [34] Ferrari, F. & Becca, F. Dynamical structure factor of the $J_1 - J_2$ Heisenberg model on the triangular lattice: magnons, spinons, and gauge fields. *Phys. Rev. X* **9**,

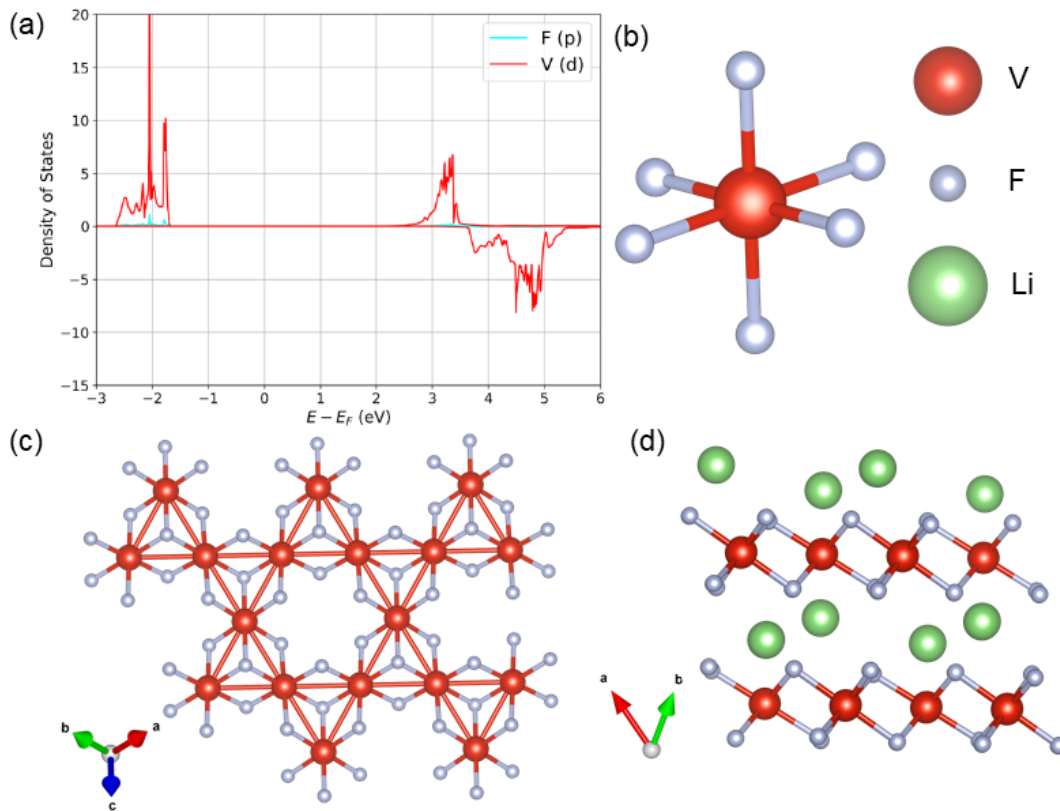


FIG. 6. (a) PDOS for $\text{Li}_2\text{V}_3\text{F}_8$ ($R\bar{3}m$). The red and cyan lines represent the V-3d and F-2p states (per atom), respectively. (b) The local atomic structure around transition-metal site (VF_6). (c) Top and (d) side view of the crystal structure. The V^{2+} ions at the centers of VF_6 octahedra adopt a t_{2g}^3 configuration ($S = 3/2$). The crystal symmetry keeps all NN bonds symmetry-equivalent, with a V-V distance of 3.14 Å.

- 031026 (2019).
- [35] Szasz, A., Wang, C. & He, Y.-C. Phase diagram of a bilinear-biquadratic spin-1 model on the triangular lattice from density matrix renormalization group simulations. *Phys. Rev. B* **106**, 115103 (2022).
- [36] Jiang, Y.-F. & Jiang, H.-C. Nature of quantum spin liquids of the $S = 1/2$ Heisenberg antiferromagnet on the triangular lattice: A parallel DMRG study. *Phys. Rev. B* **107**, L140411 (2023).
- [37] Kolley, F., Depenbrock, S., McCulloch, I. P., Schollwöck, U. & Alba, V. Phase diagram of the $J_1 - J_2$ Heisenberg model on the kagome lattice. *Phys. Rev. B* **91**, 104418 (2015).
- [38] Gong, S.-S., Zhu, W., Balents, L. & Sheng, D. Global phase diagram of competing ordered and quantum spin-liquid phases on the kagome lattice. *Phys. Rev. B* **91**, 075112 (2015).
- [39] Liao, H.-J. *et al.* Gapless spin-liquid ground state in the $S = 1/2$ kagome antiferromagnet. *Phys. Rev. Lett.* **118**, 137202 (2017).
- [40] Changlani, H. J., Kochkov, D., Kumar, K., Clark, B. K. & Fradkin, E. Macroscopically degenerate exactly solvable point in the spin-1/2 kagome quantum antiferromagnet. *Phys. Rev. Lett.* **120**, 117202 (2018).
- [41] Prelovšek, P., Morita, K., Tohyama, T. & Herberich, J. Vanishing Wilson ratio as the hallmark of quantum spin-liquid models. *Phys. Rev. Res.* **2**, 023024 (2020).
- [42] Iqbal, Y. *et al.* Gutzwiller projected states for the $J_1 - J_2$ Heisenberg model on the Kagome lattice: Achievements and pitfalls. *Phys. Rev. B* **104**, 144406 (2021).
- [43] Reynolds, P. A., Figgis, B. N. & Sobolev, A. N. The Crystal Structures at 10 K of the Trigonal Salts $\text{KMIII}(\text{NH}_3)_6(\text{ClO}_4)_2\text{Cl}_2$, $\text{MIII} = \text{Os}$ and Cr , and the Possibility of Phase Transitions. *Aust. J. Chem.* **52**, 219-226 (1999).
- [44] Inami, T. Neutron powder diffraction experiments on the layered triangular-lattice antiferromagnets $\text{RbFe}(\text{MoO}_4)_2$ and $\text{CsFe}(\text{SO}_4)_2$. *J. Solid State Chem.* **180**, 2075-2079 (2007).
- [45] Hwang, J. *et al.* Successive Magnetic Phase Transitions and Multiferroicity in the Spin-One Triangular-Lattice Antiferromagnet $\text{Ba}_3\text{NiNb}_2\text{O}_9$. *Phys. Rev. Lett.* **109**, 257205 (2012).
- [46] Amuneke, N. E., Tapp, J., de la Cruz, C. R. & Möller, A. Experimental realization of a unique class of compounds: XY-antiferromagnetic triangular lattices, $\text{KAg}_2\text{Fe}[\text{VO}_4]_2$ and $\text{RbAg}_2\text{Fe}[\text{VO}_4]_2$, with ferroelectric ground states. *J. Mater. Chem.* **26**, 5930-5935 (2014).
- [47] Lewis, J., Machin, D., Newnham, I. & Nyholm, R. 380. The magnetic properties of some halides of titanium and zirconium. *J. Chem. Soc.* 2036-2041 (1962).
- [48] Nambu, Y. & Nakatsuji, S. Two-dimensional magnetism and spin-size effect in the $S = 1$ triangular antiferromagnet NiGa_2S_4 . *J. Phys. C: Solid State Phys.* **23**, 164202

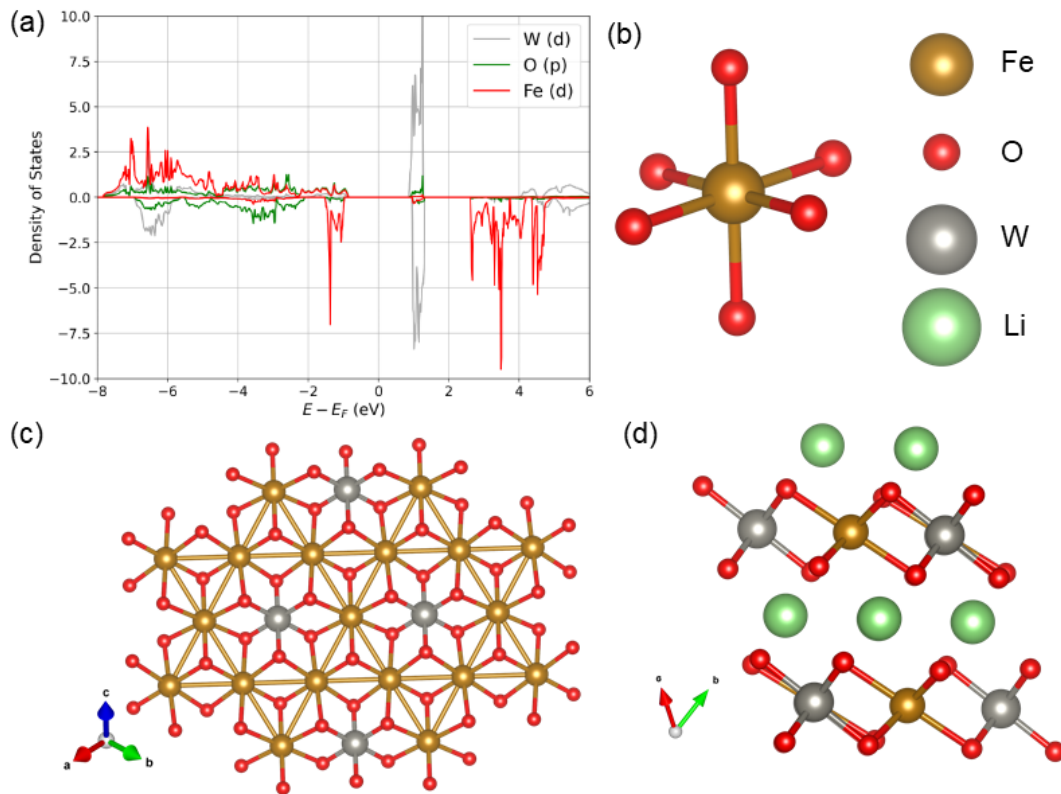


FIG. 7. (a) PDOS for $\text{Li}_4\text{Fe}_3\text{WO}_8$ ($R\bar{3}m$). The red, green and gray lines represent the Fe-3d, O-2p and W-5d states (per atom), respectively. (b) The local atomic structure around transition-metal site (FeO_6). (c) Top and (d) side view of the crystal structure. The high-spin $t_{2g}^4 e_g^2$ configuration of Fe^{2+} is captured by our calculations.

- (2011).
- [49] Mazin, I. Ab initio investigation of magnetic interactions in the frustrated triangular magnet NiGa_2S_4 . *Phys. Rev. B* **76**, 140406 (2007).
- [50] Stock, C. *et al.* Neutron-Scattering Measurement of Incommensurate Short-Range Order in Single Crystals of the $S = 1$ Triangular Antiferromagnet NiGa_2S_4 . *Phys. Rev. Lett.* **105**, 037402 (2010).
- [51] Nakatsuji, S., Nambu, Y. & Onoda, S. Novel geometrical frustration effects in the two-dimensional triangular-lattice antiferromagnet NiGa_2S_4 and related compounds. *J. Phys. Soc. Jpn.* **79**, 011003 (2010).
- [52] Zhang, K.-C., Li, Y.-F., Liu, Y. & Chi, F. Monte Carlo study of the magnetic properties of spin liquid compound NiGa_2S_4 . *Chin. Phys. B* **23**, 057501 (2014).
- [53] Pradines, B., Lacombe, L., Guih ery, N. & Suaud, N. Study of the Electronic Structure of NiGa_2S_4 and Extraction of the Spin Hamiltonian Parameters from Ab Initio Calculations. *Eur. J. Inorg. Chem.* **2018**, 503–508 (2018).
- [54] Wiesler, D. G., Suzuki, M., Suzuki, I. S. & Rosov, N. Determination of Anomalous Superexchange in MnCl_2 and Its Graphite Intercalation Compound. *Phys. Rev. Lett.* **75**, 942 (1995).
- [55] McGuire, M. A. Crystal and magnetic structures in layered, transition metal dihalides and trihalides. *Crystals* **7**, 121 (2017).
- [56] Given that it carries $S \sim 1$ moments, a more rigorous analysis is warranted, particularly beyond the bilinear Heisenberg framework. In this regime, higher-order spin interactions—such as biquadratic exchange—can play a significant role [74–77].
- [57] Freedman, D. E. *et al.* Site specific X-ray anomalous dispersion of the geometrically frustrated kagom e magnet, herbertsmithite, $\text{ZnCu}_3(\text{OH})_6\text{Cl}_2$. *J. Am. Chem. Soc.* **132**, 16185–16190 (2010).
- [58] Han, T., Chu, S. & Lee, Y. S. Refining the Spin Hamiltonian in the Spin-1/2 Kagome Lattice Antiferromagnet $\text{ZnCu}_3\text{H}_6(\text{Cl}_2)$ Using Single Crystals. *Phys. Rev. Lett.* **108**, 157202 (2012).
- [59] Fu, M., Imai, T., Han, T.-H. & Lee, Y. S. Evidence for a gapped spin-liquid ground state in a kagome Heisenberg antiferromagnet. *Science* **350**, 655–658 (2015).
- [60] Hiroi, Z. *et al.* Spin-1/2 Kagom e-Like Lattice in Volborthite $\text{Cu}_3\text{V}_2\text{O}_7(\text{OH})_2 \cdot 2\text{H}_2\text{O}$. *J. Phys. Soc. Jpn.* **70**, 3377–3384 (2001).
- [61] Kohama, Y. *et al.* Possible observation of quantum spin-nematic phase in a frustrated magnet. *Proc. Natl. Acad. Sci. U.S.A.* **116**, 10686–10690 (2019).
- [62] Colman, R. H., Ritter, C. & Wills, A. S. Toward Perfection: Kapellasite, $\text{Cu}_3\text{Zn}(\text{OH})_6\text{Cl}_2$, a New Model $S = 1/2$ Kagome Antiferromagnet. *Chem. Mater.* **20**, 6897–6899 (2008).
- [63] F ak, B. *et al.* Kapellasite: A kagome quantum spin liquid with competing interactions. *Physical review letters* **109**,

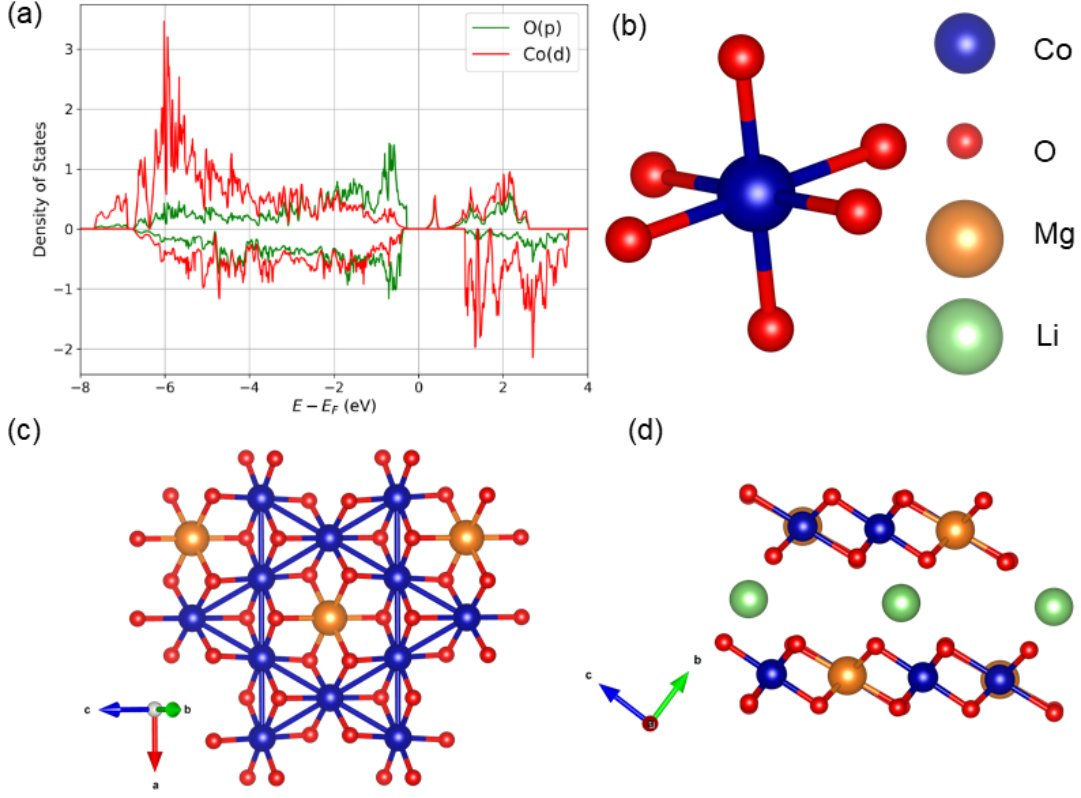


FIG. 8. (a) PDOS for $\text{Li}_2\text{MgCo}_3\text{O}_8$ ($P2/m$). The red and green lines represent the Co-3d and O-2p states (per atom), respectively. (b) The local atomic structure around transition-metal site (CoO_6). (c) Top and (d) side view of the crystal structure. Being similar with $\text{Li}_2\text{MgCo}_3\text{O}_8$ ($C2/m$), in $P2/m$ phase, the interlayer Li ions and ABC stacking lower the full crystal symmetry to monoclinic, leaving only a C_2 axis. The partial breaking of C_3 symmetry, together with slight structural distortions, splits the NN exchange into symmetry-inequivalent paths, with a maximum deviation of 0.238 and 0.203 meV in $P2/m$ and $C2/m$, respectively.

- 037208 (2012).
- [64] Janson, O., Richter, J. & Rosner, H. Modified Kagome Physics in the Natural Spin-1/2 Kagome Lattice Systems: Kapellasite $\text{Cu}_3\text{Zn}(\text{OH})_6\text{Cl}_2$ and Haydeeite $\text{Cu}_3\text{Mg}(\text{OH})_6\text{Cl}_2$. *Phys. Rev. Lett.* **101**, 106403 (2008).
- [65] Jeschke, H. O., Salvat-Pujol, F. & Valentí, R. First-principles determination of Heisenberg Hamiltonian parameters for the spin-1/2 kagome antiferromagnet $\text{ZnCu}_3(\text{OH})_6\text{Cl}_2$. *Phys. Rev. B* **88**, 075106 (2013).
- [66] Kermarrec, E. *et al.* Spin dynamics and disorder effects in the $S = 1/2$ kagome Heisenberg spin-liquid phase of kapellasite. *Phys. Rev. B* **90**, 205103 (2014).
- [67] No long-range order down to 1.6K [78, 79]; low- T trimerization ($R\bar{3}m \rightarrow R3m$, 179–190K) likely requires magnetoelastic couplings and non-Heisenberg interactions.
- [68] Large moment $\sim 5 \mu_B/\text{Mn}$; two incommensurate orders at 1.6 and 0.6 K [80]; weak J_1 - J_2 with sizable dipolar (and possibly weak interlayer) couplings likely drive the ordering.
- [69] Computed on high-symmetry $R\bar{3}m$ (Material Project); experimentally undergoes $R\bar{3}m \rightarrow P2_1/m$ below T_N well above AFM order [81], reconciling small $J_{2,3}$ from the undistorted phase.
- [70] Similar to $\text{Cs}_2\text{ZrCu}_3\text{F}_{12}$, AFM appears after $R\bar{3}m \rightarrow P2_1/n$ above T_N [82]; Materials Project lists the high-symmetry $R\bar{3}m$ used in our mapping.
- [71] Database assumes uniform Ni-Ni spacing; experiment reports inequivalent Ni-Ni distances [83].
- [72] Changlani, H. J. & Läuchli, A. M. Trimerized ground state of the spin-1 Heisenberg antiferromagnet on the kagome lattice. *Phys. Rev. B* **91**, 100407 (2015).
- [73] Messio, L., Lhuillier, C. & Misguich, G. Lattice symmetries and regular magnetic orders in classical frustrated antiferromagnets. *Phys. Rev. B* **83**, 184401 (2011).
- [74] Läuchli, A., Mila, F. & Penc, K. Quadrupolar Phases of the $S = 1$ Bilinear-Biquadratic Heisenberg Model on the Triangular Lattice. *Phys. Rev. Lett.* **97**, 087205 (2006).
- [75] Moreno-Cardoner, M., Perrin, H., Paganelli, S., De Chiara, G. & Sanpera, A. Case study of the uniaxial anisotropic spin-1 bilinear-biquadratic Heisenberg model on a triangular lattice. *Phys. Rev. B* **90**, 144409 (2014).
- [76] Niesen, I. & Corboz, P. A tensor network study of the complete ground state phase diagram of the spin-1 bilinear-biquadratic Heisenberg model on the square lattice. *SciPost Phys.* **3**, 030 (2017).
- [77] Niesen, I. & Corboz, P. Ground-state study of the spin-1 bilinear-biquadratic Heisenberg model on the triangular lattice using tensor networks. *Phys. Rev. B* **97**, 245146 (2018).

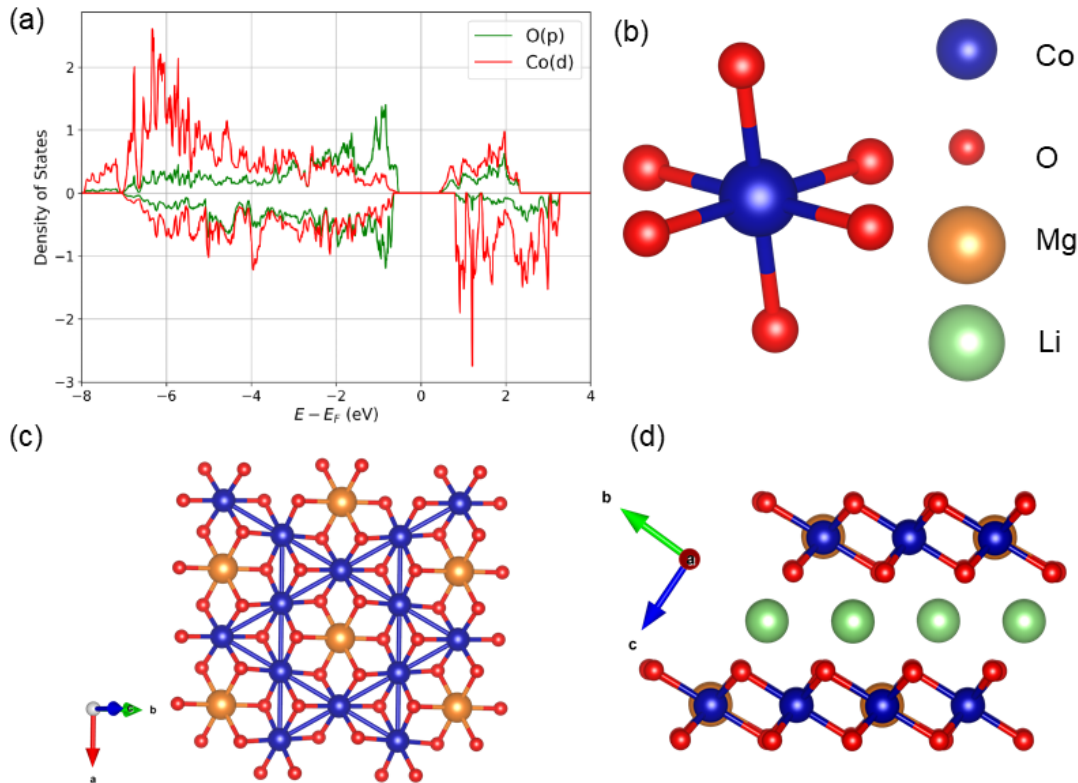


FIG. 9. (a) PDOS for $\text{Li}_2\text{MgCo}_3\text{O}_8$ ($C2/m$). The red and green lines represent the Co-3d and O-2p states (per atom), respectively. (b) The local atomic structure around transition-metal site (CoO_6). (c) Top and (d) side view of the crystal structure. Our DFT+ U calculations capture their low-spin t_{2g}^5 configuration of Co^{4+} . A single kagome-like layer comprises edge-sharing CoO_6 octahedra, with Mg located at the center of each hexagonal plaquette.

- [78] Hänni, N., Frontzek, M., Hauser, J., Cheptiakov, D. & Krämer, K. Low temperature phases of $\text{Na}_2\text{Ti}_3\text{Cl}_8$ revisited. *Z. Anorg. Allg. Chem.* **643**, 2063–2069 (2017).
- [79] Kelly, Z. A., Tran, T. T. & McQueen, T. M. Nonpolar-topolar trimerization transitions in the $S = 1$ Kagomé magnet $\text{Na}_2\text{Ti}_3\text{Cl}_8$. *Inorg. Chem.* **58**, 11941–11948 (2019).
- [80] Paddison, J. A. *et al.* Multiple incommensurate magnetic states in the kagome antiferromagnet $\text{Na}_2\text{Mn}_3\text{Cl}_8$. *Phys. Rev. B* **108**, 054423 (2023).
- [81] Reisinger, S. A., Tang, C. C., Thompson, S. P., Morrison, F. D. & Lightfoot, P. Structural phase transition in the $S = 1/2$ kagome system $\text{Cs}_2\text{ZrCu}_3\text{F}_{12}$ and a comparison to the valence-bond-solid phase in $\text{Rb}_2\text{SnCu}_3\text{F}_{12}$. *Chem. Mater.* **23**, 4234–4240 (2011).
- [82] Matan, K. *et al.* Magnetic structure and high-field magnetization of the distorted kagome lattice antiferromagnet $\text{Cs}_2\text{Cu}_3\text{SnF}_{12}$. *Phys. Rev. B* **99**, 224404 (2019).
- [83] Freedman, D. E. *et al.* Frustrated magnetism in the $S = 1$ kagomé lattice $\text{BaNi}_3(\text{OH})_2(\text{VO}_4)_2$. *Chem. Commun.* **48**, 64–66 (2012).
- [84] Ozaki, T. *et al.* OpenMX: Open source package for Material eXplorer. URL: www.openmx-square.org (2009).
- [85] Perdew, J. P. *et al.* Atoms, molecules, solids, and surfaces: Applications of the generalized gradient approximation for exchange and correlation. *Phys. Rev. B* **46**, 6671 (1992).
- [86] Dudarev, S. L., Botton, G. A., Savrasov, S. Y., Humphreys, C. & Sutton, A. P. Electron-energy-loss spectra and the structural stability of nickel oxide: An LSDA+ U study. *Phys. Rev. B* **57**, 1505 (1998).
- [87] Han, M. J., Ozaki, T. & Yu, J. O(N) LDA+ U electronic structure calculation method based on the nonorthogonal pseudoatomic orbital basis. *Phys. Rev. B* **73**, 045110 (2006).
- [88] Moore, G. C. *et al.* High-throughput determination of Hubbard U and Hund J values for transition metal oxides via the linear response formalism. *Phys. Rev. Mater.* **8**, 014409 (2024).
- [89] Liechtenstein, A., Anisimov, V. I. & Zaanen, J. Density-functional theory and strong interactions: Orbital ordering in Mott-Hubbard insulators. *Phys. Rev. B* **52**, R5467 (1995).
- [90] Ryee, S. & Han, M. J. The effect of double counting, spin density, and Hund interaction in the different DFT+ U functionals. *Sci. Rep.* **8**, 9559 (2018).
- [91] Chen, J., Millis, A. J. & Marianetti, C. A. Density functional plus dynamical mean-field theory of the spin-crossover molecule $\text{Fe}(\text{phen})_2(\text{NCS})_2$. *Phys. Rev. B* **91**, 241111 (2015).
- [92] Park, H., Millis, A. J. & Marianetti, C. A. Density functional versus spin-density functional and the choice of correlated subspace in multivariable effective action theories of electronic structure. *Phys. Rev. B* **92**, 035146 (2015).
- [93] Chen, H. & Millis, A. J. Spin-density functional theories and their + U and + J extensions: A comparative study

KMgNiO ₆ (<i>P312</i>)	$J_H = 0.496$ eV	$J_H = 0.682$ eV	$J_H = 0.868$ eV	
$U = 6.646$ eV	0.120	0.108	0.097	J_1 (meV)
	0.021	0.018	0.016	J_2 (meV)
	0.000	0.000	0.000	J_3 (meV)
$U = 5.849$ eV	0.143	0.127	0.114	J_1 (meV)
	0.025	0.023	0.020	J_2 (meV)
	0.000	0.000	0.000	J_3 (meV)
$U = 5.052$ eV	0.171	0.151	0.135	J_1 (meV)
	0.031	0.028	0.025	J_2 (meV)
	0.000	0.000	0.000	J_3 (meV)

TABLE IV. The calculated exchange interactions $J_{1,2,3}$ for KMgNiO₆ (*P312*) with varying U and J_H values [99]. In this validity check calculations, charge-DFT plus U and J_H functional originally suggested by Liechtenstein et al was used as described in Method part. While the absolute values of the exchange couplings vary by approximately a factor of two, depending on the specific functional and U - J_H parameter choices, the relative magnitudes between J_1 and J_2 remain consistent, preserving the material's position near the stripe-ordered regime in the phase diagram.

Li ₅ VP ₂ (O ₄ F) ₂ (<i>P3</i>)	$J_H = 0.437$ eV	$J_H = 0.599$ eV	$J_H = 0.761$ eV	
$U = 4.594$ eV	0.081	0.070	0.062	J_1 (meV)
	0.000	0.000	0.000	J_2 (meV)
	0.000	0.000	0.000	J_{3a} (meV)
	0.000	0.000	0.000	J_{3d} (meV)
$U = 4.123$ eV	0.091	0.079	0.069	J_1 (meV)
	0.000	0.000	0.000	J_2 (meV)
	0.000	0.000	0.000	J_{3a} (meV)
	0.000	0.000	0.000	J_{3d} (meV)
$U = 3.652$ eV	0.103	0.089	0.077	J_1 (meV)
	0.000	0.000	0.000	J_2 (meV)
	0.000	0.000	0.000	J_{3a} (meV)
	0.000	0.000	0.000	J_{3d} (meV)

TABLE V. The calculated exchange interactions $J_{1,2,3}$ for Li₅VP₂(O₄F)₂ (*P3*) with varying U and J_H values.

Li ₂ V ₃ F ₈ ($R\bar{3}m$)	$J_H = 0.437$ eV	$J_H = 0.599$ eV	$J_H = 0.761$ eV	
$U = 4.594$ eV	0.900	0.655	0.444	J_1 (meV)
	-0.034	-0.036	-0.038	J_2 (meV)
	-0.016	-0.016	-0.015	J_{3a} (meV)
	-0.006	-0.007	-0.007	J_{3d} (meV)
$U = 4.123$ eV	1.327	1.042	0.800	J_1 (meV)
	-0.033	-0.034	-0.036	J_2 (meV)
	-0.018	-0.017	-0.016	J_{3a} (meV)
	-0.005	-0.006	-0.007	J_{3d} (meV)
$U = 3.652$ eV	1.799	1.456	1.173	J_1 (meV)
	-0.032	-0.033	-0.035	J_2 (meV)
	-0.022	-0.019	-0.017	J_{3a} (meV)
	0.005	0.006	0.007	J_{3d} (meV)

TABLE VI. The calculated exchange interactions $J_{1,2,3}$ for Li₂V₃F₈ ($R\bar{3}m$) with varying U and J_H values.

$\text{Li}_2\text{Fe}_3\text{WO}_8$ ($R\bar{3}m$)	$J_H = 0$ eV	$J_H = 0.279$ eV	$J_H = 0.657$ eV	
$U = 5.485$ eV	2.386	1.614	1.152	J_1 (meV)
	0.017	0.017	0.011	J_2 (meV)
	-0.047	-0.031	-0.030	J_{3a} (meV)
	0.858	0.428	0.194	J_{3d} (meV)
$U = 4.659$ eV	3.372	2.047	1.374	J_1 (meV)
	0.000	0.020	0.014	J_2 (meV)
	-0.098	-0.038	-0.029	J_{3a} (meV)
	1.273	0.555	0.222	J_{3d} (meV)
$U = 3.833$ eV	5.724	2.773	1.690	J_1 (meV)
	-0.086	0.021	0.017	J_2 (meV)
	-0.364	-0.066	-0.031	J_{3a} (meV)
	1.839	0.742	0.249	J_{3d} (meV)

TABLE VII. The calculated exchange interactions $J_{1,2,3}$ for $\text{Li}_2\text{Fe}_3\text{WO}_8$ ($R\bar{3}m$) with varying U and J_H values.

$\text{Li}_2\text{MgCo}_3\text{O}_8$ ($P2/m$)	$J_H = 0.268$ eV	$J_H = 0.560$ eV	$J_H = 0.852$ eV	
$U = 5.767$ eV	5.262	4.143	3.296	J_1 (meV)
	2.190	1.124	0.462	J_2 (meV)
	0.562	0.319	0.301	J_{3a} (meV)
	-0.121	-0.087	-0.035	J_{3d} (meV)
$U = 5.159$ eV	6.439	5.196	4.123	J_1 (meV)
	3.473	1.874	0.886	J_2 (meV)
	1.011	0.507	0.338	J_{3a} (meV)
	-0.211	-0.160	-0.091	J_{3d} (meV)
$U = 4.551$ eV	7.820	6.477	5.354	J_1 (meV)
	5.138	2.911	1.506	J_2 (meV)
	1.746	0.837	0.452	J_{3a} (meV)
	-0.323	-0.284	-0.187	J_{3d} (meV)

TABLE VIII. The calculated exchange interactions $J_{1,2,3}$ for $\text{Li}_2\text{MgCo}_3\text{O}_8$ ($P2/m$) with varying U and J_H values.

- of transition metals and transition metal oxides. *Phys. Rev. B* **93**, 045133 (2016).
- [94] Jang, S. W., Ryee, S., Yoon, H. & Han, M. J. Charge density functional plus U theory of LaMnO_3 : Phase diagram, electronic structure, and magnetic interaction. *Phys. Rev. B* **98**, 125126 (2018).
- [95] Jang, S. W. *et al.* Hund's physics and the magnetic ground state of CrOX ($X = \text{Cl}, \text{Br}$). *Phys. Rev. Mater.* **5**, 034409 (2021).
- [96] Yoon, H. *et al.* Reliability and applicability of magnetic-force linear response theory: Numerical parameters, predictability, and orbital resolution. *Phys. Rev. B* **97**, 125132 (2018).
- [97] Yoon, H., Kim, T. J., Sim, J.-H. & Han, M. J. Jx: An open-source software for calculating magnetic interactions based on magnetic force theory. *Comput. Phys. Commun.* **247**, 106927 (2020).
- [98] Szilva, A. *et al.* Quantitative theory of magnetic interactions in solids. *Rev. Mod. Phys.* **95**, 035004 (2023).
- [99] Ryee, S. & Han, M. J. The effect of double counting, spin density, and Hund interaction in the different DFT+ U functionals. *Sci. Rep.* **8**, 9559 (2018).
- [100] Gong, S.-S., Zhu, W. & Sheng, D. N. Emergent Chiral Spin Liquid: Fractional Quantum Hall Effect in a Kagome Heisenberg Model. *Sci. Rep.* **4**, 6317 (2014).
- [101] Bieri, S., Lhuillier, C. & Messio, L. Projective symmetry group classification of chiral spin liquids. *Phys. Rev. B* **93**, 094437 (2016).
- [102] Sun, R.-Y., Jin, H.-K., Tu, H.-H. & Zhou, Y. Possible chiral spin liquid state in the $S = 1/2$ kagome Heisenberg model. *npj Quantum Mater.* **9**, 16 (2024).
- [103] Hu, W.-J. *et al.* Variational Monte Carlo study of a chiral spin liquid in the extended Heisenberg model on the kagome lattice. *Phys. Rev. B* **91**, 041124 (2015).
- [104] Sun, R.-Y., Jin, H.-K., Tu, H.-H. & Zhou, Y. Possible chiral spin liquid state in the $S = 1/2$ kagome Heisenberg model. *npj Quantum Mater.* **9**, 16 (2024).
- [105] Gong, S.-S., Zhu, W., Balents, L. & Sheng, D. N. Global phase diagram of competing ordered and quantum spin-liquid phases on the kagome lattice. *Phys. Rev. B* **91**, 075112 (2015).
- [106] Wietek, A., Sterdyniak, A. & Läuchli, A. M. Nature of chiral spin liquids on the kagome lattice. *Phys. Rev. B* **92**, 125122 (2015).
- [107] Messio, L., Bernu, B. & Lhuillier, C. Kagome Antiferromagnet: A Chiral Topological Spin Liquid? *Phys. Rev. Lett.* **108**, 207204 (2012).
- [108] Kiese, D. *et al.* Pinch-points to half-moons and up in the stars: The kagome skymap. *Phys. Rev. Res.* **5**, L012025 (2023).
- [109] Lugan, T., Jaubert, L. D. C., Udagawa, M. & Ralko, A. Schwinger boson theory of the $J_1, J_2 = J_3$ kagome antiferromagnet. *Phys. Rev. B* **106**, L140404 (2022).
- [110] Mizoguchi, T., Jaubert, L. D. C. & Udagawa, M. Clustering of Topological Charges in a Kagome Classical Spin Liquid. *Phys. Rev. Lett.* **119**, 077207 (2017).
- [111] Mizoguchi, T., Jaubert, L. D. C., Moessner, R. & Udagawa, M. Magnetic clustering, half-moons, and shadow pinch points as signals of a proximate Coulomb phase in frustrated Heisenberg magnets. *Phys. Rev. B* **98**, 144446 (2023).

$\text{Li}_2\text{MgCo}_3\text{O}_8$ ($C2/m$)	$J_{\text{H}} = 0.268$ eV	$J_{\text{H}} = 0.560$ eV	$J_{\text{H}} = 0.852$ eV	
$U = 5.767$ eV	5.464	4.258	3.370	J_1 (meV)
	2.079	1.112	0.497	J_2 (meV)
	0.476	0.267	0.253	J_{3a} (meV)
	-0.114	-0.085	-0.026	J_{3d} (meV)
$U = 5.159$ eV	6.803	5.363	4.249	J_1 (meV)
	3.266	1.806	0.885	J_2 (meV)
	0.882	0.435	0.278	J_{3a} (meV)
	-0.192	-0.156	-0.086	J_{3d} (meV)
$U = 4.551$ eV	8.299	6.663	5.376	J_1 (meV)
	4.699	2.736	1.458	J_2 (meV)
	1.538	0.732	0.382	J_{3a} (meV)
	-0.241	-0.261	-0.181	J_{3d} (meV)

TABLE IX. The calculated exchange interactions $J_{1,2,3}$ for $\text{Li}_2\text{MgCo}_3\text{O}_8$ ($C2/m$) with varying U and J_{H} values.

- (2018).
- [112] Bernu, B., Pierre, L., Essafi, K. & Messio, L. Effect of perturbations on the kagome $S = \frac{1}{2}$ antiferromagnet at all temperatures. *Phys. Rev. B* **101**, 140403 (2020).
- [113] Grison, V., Viot, P., Bernu, B. & Messio, L. Emergent Potts order in the kagome $J_1 - J_3$ Heisenberg model. *Phys. Rev. B* **102**, 214424 (2020).
- [114] Bose, A., Haldar, A., Sørensen, E. S. & Paramakanti, A. Chiral broken symmetry descendants of the kagome lattice chiral spin liquid. *Phys. Rev. B* **107**, L020411 (2023).
- [115] Buessen, F. L. & Trebst, S. Competing magnetic orders and spin liquids in two- and three-dimensional kagome systems: Pseudofermion functional renormalization group perspective. *Phys. Rev. B* **94**, 235138 (2016).
- [116] Li, T. A continuous family of fully frustrated Heisenberg models on the Kagome lattice. *EPL* **133**, 47001 (2021).
- [117] Iqbal, Y. *et al.* Paramagnetism in the kagome compounds $(\text{Zn, Mg, Cd})\text{Cu}_3(\text{OH})_6\text{Cl}_2$. *Phys. Rev. B* **92**, 220404 (2015).
- [118] Messio, L., Lhuillier, C. & Misguich, G. Lattice symmetries and regular magnetic orders in classical frustrated antiferromagnets. *Phys. Rev. B* **83**, 184401 (2011).
- [119] Henley, C. L. The “Coulomb Phase” in Frustrated Systems. *Annu. Rev. Condens. Matter Phys.* **1**, 179–210 (2010).
- [120] Given that it carries $S \sim 1$ moments, a more rigorous analysis is warranted, particularly beyond the bilinear Heisenberg framework. In this regime, higher-order spin interactions—such as biquadratic exchange—can play a significant role [74–77].
- [121] No long-range order down to 1.6 K [78, 79]; low- T trimerization ($R\bar{3}m! \rightarrow R3m$, 179–190 K) likely requires magnetoelastic couplings and non-Heisenberg interactions.
- [122] Large moment $\sim 5 \mu_{\text{B}}/\text{Mn}$; two incommensurate orders at 1.6/0.6 K [80]; weak $J_1 - J_2$ with sizable dipolar (and possibly weak interlayer) couplings likely drive the ordering.
- [123] Computed on high-symmetry $R\bar{3}m$ (Materials Project); experimentally undergoes $R\bar{3}m \rightarrow P2_1/m$ below T_{N} well above AFM order [81], reconciling small $J_{2,3}$ from the undistorted phase.
- [124] Similar to $\text{Cs}_2\text{ZrCu}_3\text{F}_{12}$, AFM appears after $R\bar{3}m \rightarrow P2_1/n$ above T_{N} [82]; Materials Project lists the high-symmetry $R\bar{3}m$ used in our mapping.
- [125] Database assumes uniform Ni–Ni spacing; experiment reports inequivalent Ni–Ni distances [83].